The theoretical study of ion insertion and transport in energy storage materials

Inaugural-Dissertation
to obtain the academic degree
Doctor rerum naturalium (Dr. rer. nat.)
submitted to the Department of Biology, Chemistry and Pharmacy
of Freie Universität Berlin

by

Qian Zhang

October 23, 2018

This thesis was prepared under the supervison of Dr. Payam Kaghazchi at Freie Universität Berlin from September 2014 until September 2018.

The originality of this work is confirmed by the author.

Reviewer 1: Dr. Payam Kaghazchi

Reviewer 2: Prof. Dr. Beate Paulus

Freie Universität Berlin
Physikalische und Theoretische Chemie
Institut für Chemie und Biochemie

Date of defence: October 04$^{\text{th}}$, 2018

Abstract

The increasing demand of energy storages for the portable electric devices and electric vehicles has promoted extensive research on high power density as well as long cycle and calendar life rechargeable energy systems such as Li-ion batteries, Na-ion batteries, Mg-ion batteries and Al-ion batteries. First-principle calculations are valuable in understanding and designing high-performance battery materials. In this thesis, DFT method together with thermodynamic and kinetic approaches has been applied to study the following properties and processes of electrode materials: i) insertion and transport of Li ion in TiO_2-B, ii) formation and migration of charge carriers in LiX (X = I, Br, and Cl), iii) intercalation of $AlCl_4^-$ into graphite, and iv) effect of dopant on the properties of $LiNiO_2$. Our studies on the first and second systems show that, depending on the type of materials, kinetic or thermodynamic factor plays key role in determining the specific capacity and ionic conductivity. By calculating the diffusion length of Li as a function of C-rate, we find that the energy barrier of Li transport controls the size-sensitivity of capacity in TiO_2-B, which is widely studied as anode in Li-ion battery. However, the calculated activation energies of Li ion in LiX, which can be components of solid electrolyte interphase layer in Li-ion battery, show that the ionic conductivity is determined by the defect formation energy (concentration) and not by diffusion barrier. A comparison between our simulated XRD pattern and experimental ones from our collaborator for a novel Al-ion battery shows that reversible insertion of $AlCl_4^-$ into graphite cathode occurs via staging mechanism from stage 6 to stage 3 during the charge process. Our combined theoretical-experimental study for Zr doping of $LiNiO_2$, which is a promising cathode of next generation Li-ion battery, shows that low-level doping will promote the cation mixing in $LiNiO_2$ but not change the Li vacancy formation energy.

Abstrakt

Der steigende Bedarf an Energiespeichern für portable elektronische Geräte und Elektrofahrzeuge hat eine umfangreiche Forschung zur Entwicklung neuartiger wiederaufladbarer Batterien mit hoher Leistungsdichte sowie langer Zyklus- und Kalenderlebensdauer ausgelöst. *Ab-initio* Berechnungen sind wertvolle Werkzeuge für das Verständnis und die Entwicklung von Hochleistungs-Batteriematerialien. In dieser Dissertation wurde die DFT-Methode zusammen mit thermodynamischen und kinetischen Methoden verwendet, um die folgenden Eigenschaften und Prozesse von Elektrodenmaterialien zu untersuchen: i) Insertion und Transport von Li-Ionen in TiO_2-B, ii) Bildung und Migration von Ladungsträgern in LiX (X = I, Br und Cl), iii) Interkalation von $AlCl_4^-$ in Grafit und iv) Effekt des Dotanden auf die Eigenschaften von $LiNiO_2$. Unsere Untersuchungen am ersten und zweiten Punkt zeigen, dass in Abhängigkeit von der Art der Materialien die kinetischen oder thermodynamischen Faktoren Schlüsselrollen bei der Bestimmung der spezifischen Kapazität und Ionenleitfähigkeit spielen. Die Verwendung von TiO_2-B resultierte dabei von der Tatsache, dass dieser Stoff bereits häufig untersucht wurde und daher ein gutes Ausgangsmaterial darstellt. Durch die Berechnung der Diffusionslänge von Li als Funktion der C-Rate (Ladungsdauer) haben wir herausgefunden, dass die Energiebarriere des Li-Transports die Abhängigkeit der Kapazität von der Nanopartikelgröße von TiO_2-B steuert. Die berechneten Aktivierungsenergien von Li-Ionen in LiX, die die Komponenten der Festelektrolyt-Zwischenphasenschicht in Li-Ionen-Batterien sind, zeigen jedoch, dass die Ionenleitfähigkeit durch die Defektbildungsenergie (d. h. Konzentration) und nicht durch die Diffusionsbarriere (d. h. Diffusionskoeffizient) bestimmt wird. Ein Vergleich zwischen unseren simulierten XRD-Mustern und den experimentellen Ergebnissen unserer Kooperationspartner für eine neuartige Al-Ionen-Batterie zeigt, dass die reversible Insertion von $AlCl_4^-$ in die Grafitkathode über den Staging-Mechanismus von Stufe 6 bis Stufe 3 erfolgt. Unsere kombinierte theoretisch-experimentelle Studie zur Zr-Dotierung von $LiNiO_2$, einer vielversprechenden Kathode für Li-Ionen-Batterien der nächsten Generation, zeigt, dass eine Zr Dotierung mit niedrigem Niveau die Kationenmischung in LiNiO2 fördert, aber nicht die Bildungsenergie von Li-Leerstellen verändert.

List of Publications

A1

"Strong Li-Content Dependence of Li Diffusivity in TiO_2-B"

Qian Zhang and Payam Kaghazchi

J. Phys. Chem. C, 120(2016), pp. 22163-22168

DOI: 10.1021/acs.jpcc.6b06319

A2

"Dependence of Ion Transport on the Electronegativity of the Constituting Atoms in Ionic Crystals"

Qian Zhang and Payam Kaghazchi

ChemPhysChem, 18(2017), pp. 965-969

DOI: 10.1002/cphc.201601208

A3

"An operando X-ray diffraction study of chloroaluminate anion-graphite intercalation in aluminum batteries"

Chun-Jern Pan, Chunze Yuan, Guanzhou Zhu, Qian Zhang Chen-Jui Huang, Meng-Chang Lin, Michael Angell, Bing-Joe Hwang, Payam Kaghazchi, and Hongjie Dai

PNAS, 115(2018), pp. 5670-5675

DOI: 10.1073/pnas.1803576115

A4

"Cation Ordering of Zr-Doped $LiNiO_2$ Cathode for Lithium-Ion Batteries"

Chong S. Yoon, Min-Jae Choi, Do-Wook Jun, Qian Zhang, Payam Kaghazchi, Kwang-Ho Kim, and Yang-Kook Sun

Chem. Mater., 30(2018), pp. 1808-1814

DOI: 10.1021/acs.chemmater.8b00619

Additional publications

D1

"Pushing the limit of layered transition metal oxide cathodes for high-energy density rechargeable Li ion batteries"

U.-H. Kim, D.-W. Jun, K.-J. Park, Q. Zhang, P. Kaghazchi, D. Aurbach, D. T. Major, G. Goobes, M. Dixit, N. Leifer, C. M. Wang, P. Yan, D. Ahn, K.-H. Kim, C. S. Yoon, and Y.-K. Sun

Energy Environ. Sci., 11(2018), pp. 1271-1279

DOI: 10.1039/c8ee00227d

D2

"A robust network binder with dual functions of Cu^{2+} ions as ionic crosslinking and chemical binding agents for highly stable Li-S batteries"

Jie Liu, Minghao Sun, Qian Zhang, Feifei Dong, Payam Kaghazchi, Yanxiong Fang, Shanqing Zhang, and Zhan Lin

J. Mater. Chem. A, 6(2018), pp. 7382-7388

DOI: 10.1039/c8ta01138a

D3

"Theoretical study of superionic phase transition in Li_2S"

Sara Panahian Jand, Qian Zhang, and Payam Kaghazchi

Sci. Rep., 5873(2018)

DOI: 10.1038/s41598-017-05775-2

D4

"Inorganic-Organic Coating via Molecular Layer Deposition Enables Long Life Sodium Metal Anode"

Yang Zhao, Lyudmila V. Goncharova, Qian Zhang, Payam Kaghazchi, Qian Sun, Andrew Lushington, Biqiong Wang, Ruying Li, and Xueliang Sun

Nano Lett., 17(2018), pp. 5653-5659

DOI: 10.1021/acs.nanolett.7b02464

D5

"Understanding on the structural and electrochemical performance of orthorhombic sodium manganese oxides"

Ji Ung Choi, Chong Seung Yoon, Qian Zhang, Payam Kaghazchi, Young Hwa Jung, Kug-Seung Lee, Do-Cheon Ahn, Yang-Kook Sun, and Seung-Taek Myung

Adv. Sci., submitted

List of Abbreviation

LIB	Li-ion battery
ASSB	All-solid-state battery
DFT	Density functional theory
AIMD	Ab-initio molecular dynamic
DMC	Dimethyl carbonate
PC	Propylene carbonate
SEI	Solid electrode interphase
NCM	$LiNi_xCo_yMn_{1-x-y}$
LCO	$LiCoO_2$
LNO	$LiNiO_2$
AIB	Aluminium-ion battery
GIC	Graphite intercalation compound
XRD	X-ray powder diffraction
BOA	Born-Oppenheimer Approximation
HF	Hartree-Fock
TF	Tomas Fermi
KS	Kohn-Sham
L(S)DA	Local (spin) density approximation
GGA	Generalized Gradient Approximation
PBE	Perdew-Burke-Ernzerhof
vdWs	van der Waals
BJ	Becke-Jonson
AO	Atomic orbital
STO	Slater-type-orbital
GTO	Gaussian-type-orbital
CGF	Contracted Gaussian function
PW	Plane wave
BZ	Brillouin Zone
NCPP	Norm-conserving pseudopotential
PAW	Projector augmented wave
NEB	Nudged elastic band

MEP	Minimum energy path

List of Figures

Contents

1 Introduction

Among the commercial rechargeable batteries, Li-ion batteries (LIBs) are of the most applied energy storages for mobile application (cell phones and electric vehicles) due to their relatively high gravimetric (250 Wh/kg) and volumetric energy density (650 Wh/L) and low self-discharge property [1, 2]. However, there are several issues left, which hinder further application of LIBs in electric vehicles [2], such as the limited cycle life, the high cost and the poor performance at high temperature. Therefore, an extensive research on LIBs is still going on to solve these problems and improve the limitations. At the same time, other novel rechargeable batteries such as Li-air battery, Li-S battery, solid-state battery, and Al-ion battery also attract researchers' interest because of their advantages in some ways compared to LIBs. An overview about on going researches on different energy storages is given in the following:

(i) **Li-ion battery**. LIB works via Li^+ transport through electrolyte and intercalation into cathode (*e.g.* $LiCoO_2$) or anode (*e.g.* graphite) during charge and discharge. The energy density of LIBs can be improved by developing either high voltage cathode active materials [3, 4] or high capacity anode electrode materials [5, 6]. Experimentally, this can be realized for example by i) developing new materials, ii) doping or substituting external elements in electrode [7, 8], and iii) controlling the size [9, 10], shape and structure such as nanowire [11, 12], naosheet [13], and nanotube [14].

(ii)**Li-Air battery**. Li-air batteries use porous air electrode (*e.g.* mesoporous carbon) as cathode and metallic Li as anode. Li-air battery works through oxidation of Li at the anode and reduction of O_2 at the cathode during discharge. Li-air batteries have the highest specific energy (1000–2000 Wh/kg) among all the rechargeable batteries. However, the stability of Li-air battery is poor due to the high reactivity of lithium [15, 16]. Moreover, the formation of LiOH and Li_2CO_3 due to the reaction of lithium with H_2O and CO_2 as well as the reaction between cathode and the lithium peroxide prevent the recharge of Li-air battery. Study of Li-air battery is still at an early stage.

(iii) **Li-S battery**. Li-S batteries use S-based material as cathode and metallic Li as anode. Li-S battery works based on the oxidation of Li metal at anode and the reduction of S-based material at cathode during discharge. Li-S battery has a theoretical specific energy of $\sim$750 Wh/kg [17] which is lower than Li-air battery, but higher than Li-ion battery. Li-S batteries are considered to be a suitable substitution for LIBs because

of their relatively high theoretical specific energy density and low cost [18]. The main problem of Li-S battery is the low electrical conductivity of S cathode which results in rapid capacity fading on cycling [19]. The current research on Li-S batteries focuses on finding highly conductive cathodes [20, 21].

(iv)**All-solid-state battery (ASSB)**. ASSBs have similar working principle as LIBs. However, instead of using liquid-state materials, solid-state battery uses solid-state materials as electrolyte. ASSB has a high specific energy density as well as high thermal and chemical stability [22]. Moreover, ASSB allows faster recharging and longer cycle life of electric vehicles. The main problems faced to solid-state battery are the high manufacture cost and the difficulty to maintain the contact between the solid electrolyte and electrodes.

(v)**Al-ion battery**. Al-ion batteries use metallic Al, graphite (an example) and ionic liquid (chloroaluminate salts) as anode, cathode and electrolyte, respectively. Al-ion batteries work through the electrochemical deposition and dissolution of Al at the anode and the intercalation/de-intercalation of $AlCl_4^-$ anions in the cathode. Al-ion battery has several impressive advantages such as the high theoretical gravimetric capacity (2.980 Ah/kg)(Li-ion battery: 3.862 Ah/kg and Na-ion battery:1.166 Ah/kg) [23], low cost (raw material abundance) and non-flammable property. However, there are also some disadvantages such as low capacity and low cell discharge voltage plateaus [24]. A lot of work are needed to improve the capacity and increase the discharge voltage plateaus before the commercialization of Al-ion battery.

Besides the large number of experimental works on different types of rechargeable battery systems, theoretical studies have also been performed based on the first-principle density functional theory (DFT) and ab-initio molecular dynamic (AIMD). Theoretical work has mainly focused on the ion insertion and transport of ions in electrodes [25–27], electrode structure distortion and phase transition during charge and discharge [28–31], surface effect [32] and dopant effect [33, 34] on performance of electrode materials et al. In this thesis, I performed theoretical investigations on four different electrode materials in Li-ion battery and Al-ion battery: (i) the insertion and transport of Li^+ ion in Li_xTiO_2-B anode, (ii) the extraction and transport of Li^+ ion in rock-salt LiX (X = I, Br, and Cl) compounds, (iii) the mechanism of $AlCl_4^-$ intercalation into graphite cathode in Al-ion battery, and (iv) the changes in atomic structure, Li vacancy formation energy and charge

compensation mechanism of $LiNiO_2$ after Zr doping. In the following, more details on Li-ion battery and Al-ion battery as well as my motivations for choosing these systems will be given.

1.1 Li-ion battery

Li-ion battery is assembled with cathode (negative) electrode, anode (positive) electrode, electrolyte and separator. Cathode and anode electrodes are separated by an electrolyte which composes of Li-contained salt (*e.g.* $LiPF_6$) dissolved into organic solvents (*e.g.* Dimethyl carbonate (DMC) and Propylene carbonate (PC)). Electrolyte enables the Li^+ to diffuse between cathode and anode during charge and discharge. Separator is an inactive material which prevents the physical contact of electrodes. As shown in Fig.1, during the discharge process, Li^+ ion migrates from anode (*e.g.* Li_xC_6) to cathode (*e.g.* $LiCoO_2$) through the organic electrolyte accompanied with a electron transfer in external circuit. During the charge process, an external voltage (higher than that produced by battery itself) needs to be applied to supply an current and force the Li^+ to migrate back to anode from cathode in order to prepare for the next discharge process. The reversible reactions in cathode and anode, respectively are

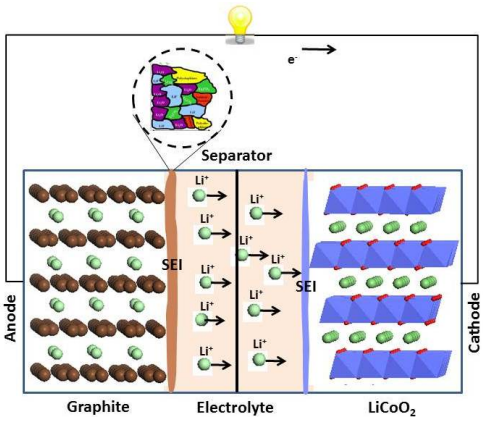

Figure 1: Schematic of the discharge process of a commercially used Li-ion battery. High magnification is the schematic components of SEI film.

$$Li_xCoO_2 \rightleftharpoons Li_{x-y}CoO_2 + yLi^+ + ye^-, \tag{1.1}$$

and

$$yLi^+ + ye^- + 6C \rightleftharpoons Li_yC_6. \tag{1.2}$$

Besides the aforementioned reversible reactions during the charge and discharge, side reactions occur between the electrolyte and the electrodes resulting in the decomposition of electrolyte and the consumption of Li^+. These side reactions form a solid electrolyte interphase (SEI) on the surface of cathode and anode, leading to the increase of impedance of electrodes and the fade of capacity. The formation of SEI is however important in LIBs

since it prevents the further decomposition of electrolyte and the corrosion of electrodes. In the following section, recent studies on each component of LIBs will be discussed in more details.

1.1.1 Anode

Due to the relative low capacity of graphite anode (372 mAh/g) in commercial LIBs, many other anode materials have been proposed and studied. The commonly-studied anodes include carbon-based materials (*e.g.* carbon nanotube and porous carbon) [35,36], Si [37], SiO [38], Ge [39], Sn [40] and Titanium oxides (*e.g.* TiO_2) [41]. Due to its relatively high theoretical capacity, good cycling stability, high safety and low cost character, TiO_2 is one of the promising candidates for graphite [10, 42]. Four different phases of TiO_2 (Rutile [43], Anatase [44], Brookite [45] and Bronze [46,47]) have been studied as anode of LIBs. Bronze TiO_2 (TiO_2-B) has a better intercalation performance and higher reversible capacity compared to other three phases [10]. This is due to its open structure with atomically-large channels [48]. TiO_2-B has a monoclinic structure with a space group of C2/m, composing of edge- and corner-sharing TiO_6 octahedrals (Fig.2). There are eight Ti sites and ten Li sites in one unit cell corresponding to a stoichiometric formula of $Li_{1.25}TiO_2$ in the case of fully occupation of Li sites and a theoretical capacity of 420 mAh/g [10, 49]. However, the highest capacity of bulk TiO_2 achieved experimentally is only 251 mAh/g, corresponding to a Li/Ti ratio of 0.75 [50]. Many theoretical works about the intercalation behavior of Li into TiO_2-B have been reported. DFT calculations by Arrouvel et al [51] found that Li prefers to insert into the center of channel (see Fig.2) and migrate along the channel with a low barrier of 0.3 eV at low Li concentration (Li/Ti<0.125) by using DFT method. With DFT and Monte Carlo simulations Van der Ven *et al.* [52] predicted the lithium site occupancies, voltage curves, and phase diagram of TiO_2-B . They found that bulk Li_xTiO_2-B with $0.75< x \leq 1.25$ is thermodynamically favorable, but the voltage drops dramatically for $x \geq 1.00$. Nevertheless, the reason for the low capacity of bulk TiO_2-B has not been reported. In this thesis, a comprehensive study of the Li insertion mechanism (pathway

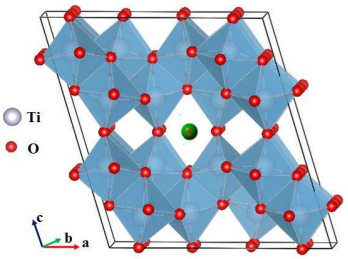

Figure 2: Atomic structure of TiO_2-B. C site (in green) is the center of channel

and energy barrier of lithiation) at different Li concentrations (Li/Ti=0-1.25) has been performed using DFT. Moreover, the maximum diffusion length as a function of C-rate was estimated. In addition, the relationship between the size of Li_xTiO_2-B particle and the capacity is predicted. The calculations show that the origin of the low capacity of bulk TiO_2-B is a kinetic limitation.

1.1.2 Cathode

Recent commonly-studied cathodes include $LiNi_xCo_yMn_{1-x-y}$ (x=0-1, y=0-1), $LiMPO_4$, LiM_2O_4 and Li_2MSiO_4 (where M represents Fe, Co, Ni, and Mn *et al.*) [53]. $LiCoO_2$ (LCO) has been commercialized since 1990 because of its high specific capacity (274 mAh/g), low self-discharge, high discharge voltage and good cycling performance. LCO has a rhombohedral structure with a $R\bar{3}m$ space group which composes of edge-sharing CoO_6 octahedral sheets sandwiched by Li layers (Fig.1).The main limitations of LCO cathode are high cost and low thermal stability [54]. Different strategies such as nano-structuring LCO [55], doping with external elements (Mn, Al, Ni, Ti, La, Mg, etc) [7,8,56], and coating metal oxides (Al_2O_3 and TiO_2, etc) [57–59] have been reported to improve the thermal stability and electrochemical performance of LCO. In particular, $LiNi_xCo_yMn_{1-x-y}O_2$ (NCM) is widely studied as a replacement of LCO due to its high specific capacity, high thermal stability and low cost [60, 61]. For example, Sun *et al.* [62] studied comprehensively the electrochemical property of $LiNi_{1/3}Co_{1/3}Mn_{1/3}O_2$, $LiNi_{0.5}Co_{0.2}Mn_{0.3}O_2$, $LiNi_{0.6}Co_{0.2}Mn_{0.2}O_2$, $LiNi_{0.70}Co_{0.15}Mn_{0.15}O_2$, $LiNi_{0.8}Co_{0.1}Mn_{0.1}O_2$, and $LiNi_{0.85}Co_{0.075}Mn_{0.075}O_2$ to clarify the role of each transition metal in NCM. He found that the increase of Ni will increase the initial discharge capacity but lead to poor cycling performance and poor thermal stability of NCM. The increase of Co will improve the cycling performance but decrease the capacity of NCM. The increase of Mn will increase the thermal stability but decrease the capacity of NCM. The poor stability of NCM with high Ni content originates from the oxygen release and cation mixing in the structure. Kondrakov et al [63] investigated the capacity-fading mechanism of $LiNi_{1/3}Co_{1/3}Mn_{1/3}$ (NCM111) with low Ni content and $LiNi_{0.8}Co_{0.1}Mn_{0.1}$(NCM811) with high Ni content. They found that NCM811 undergoes much larger volume change during cycling compared to NCM111 and shows severe microcracking. The stability of NCM cathode with high Ni content can be improved by doping or substituting elements such as Al and Mg. Cho *et al.* [64] investigated the effect of Al

and Mg dopant on preventing the degradation of NCM811 using DFT calculations. They found that Al doping can effectively prevent the formation of oxygen vacancies, while Mg doping can suppress the cation mixing and decrease the lattice parameter deformation. In this thesis, we studied the effect of Zr dopant on the atom arrangement, lattice constant and Li vacancy formation energy of $LiNiO_2$ (LNO) using DFT+U method. The charge compensate mechanism after Zr doping is also studied. Our calculations show that a low-level doping of Zr in LNO will promote the cation ordering (Ni distributes homogeneously in Li layer), but not change the Li vacancy formation energy of LNO.

1.1.3 Electrolyte

As mentioned in section 1.1, LIB works through the transport of Li^+ in electrolyte and the transport of electrons in external circuit. Therefore, electrolyte plays a key role in the LIB. A suitable electrolyte should fulfil the following conditions: (i) be a superior ionic conductor but a electronic insulator to minimize the self-discharge, (ii) be stable (no decomposition or degradation) in the working voltage range of LIBs, (iii) be inactive with the anode, cathode and current collector of LIBs, (iv) be stable in the operating temperature range.

There are mainly two types of electrolytes, which are used in LIBs. (i) Liquid electrolytes consisting of lithium salts such as $LiPF_6$ and $LiClO_4$ dissolved into organic solvent such as DMC. The organic solvent is toxic and flammable which may lead to safety problems of LIBs. The SEI formed on the surface of electrodes due to the decomposition of electrolyte will be discussed in the following section. (ii) Solid electrolytes such as ceramics, glass and lithium sulfide. Solid electrolyte has a safety advantage compared to liquid electrolyte because of its high stability under high temperature and high pressure. Many companies such as BMW and Toyota have started their researches on solid electrolytes at this time.

1.1.4 Solid electrolyte interphase (SEI)

SEI is a very complicated layer consisting of inorganic components which are the decomposition products of lithium salt and organic components in the electrolyte. The types of SEI components depend closely on the species of salt and organic solvent in the liquid electrolyte. The major components of SEI include LiF, Li_2CO_3 [65], Li_2O [66], $(CH_2OCO_2Li)_2$, $ROCO_2Li$, ROLi [67], and LiOH [68]. The ion transport property of SEI,

therefore, mainly depends on the ionic conductivity of inorganic components *e.g.* LiF, Li_2CO_3 and Li_2O. Understanding the Li migration mechanism of these components is important for understanding the Li ion transport property of LIBs. Many works about the Li transport in LiF, Li_2CO_3 and Li_2O have been reported with DFT method [69, 70]. Chen et al [71] calculated the diffusion barriers of these three compounds with DFT. Li ion migration in Li_2CO_3 and Li_2O is high with diffusion barrier of 0.227 and 0.152 eV, respectively. However, the Li diffusion in LiF crystal is relatively slow with a diffusion barrier of 0.729 eV. Other inorganic components such as lithium halides may also exist in the SEI because of the additives in electrolyte or the halogen doping in the electrode materials. PC is a high Li ion conducting electrolyte. However, it decomposes at a lower potential than that of Li ion intercalation into graphite. Halogenated additives such as $BrCH(CH_2)CO_2$ and $ClCO_2CH_3$ can dramatically increase the decomposition potential of PC (from 0.9 V to 1.7 V) [72]. With these additives, LiCl and LiBr will also form as a component of SEI. Zhao et al [73] doped halogen elements (I, Br, and Cl) in $LiCoO_2$ cathode, which increased the structure stability and Li mobility of $LiCoO_2$. Moreover, LiX (X = I, Br, and Cl) have been widely used as component of electrolyte in ASSBs [74, 75]. The ionic conductivity is determined by the activation energy E_a (sum of defect formation energy ΔE_f and defect diffusion barrier ΔE_b) of the defects (charge carriers) in crystal. To my knowledge, the relation between E_a and fundamental properties of elements in solids has not been studied using DFT. In this thesis, we calculated the Li transport as a function of Li chemical potential (i.e. voltage) in LiX using DFT method. A transition from intrinsic to p-type regime occurs in LiX below a certain Li chemical potential leading to a change of Li transport mechanism and E_a value. A linear relation between E_a (in the intrinsic regime) and the Gibbs energy of formation of LiX was also found.

1.2 Al-ion battery(AIB)

Due to the high cost of Li metal for Li based batteries, other rechargeable batteries with greater earth abundance and lower cost materials such as Na-ion batteries [76, 77], Mg-ion batteries [78], Zn-ion batteries [79], Ca-ion batteries [80] and Al-ion batteries [81, 82] have been developed. Similar to LIB, AIB also consists of anode (Al metal), electrolyte (chloroaluminate salts ($AlCl_4^-$) obtained by mixing of $AlCl_3$ and complex chloride ionic liquid (e.g. 1-ethyl-3-methylimidazolium chloride([EMIm]Cl)) and cathode. Several ma-

terials have been reported as cathode of AIB, such as V_2O_5 [83], fuorinated natural graphite [84], and anatase TiO_2 [85]. AIB works through the oxide/reduction reaction of Al anode with $AlCl_4^-$ in electrolyte accompanied with 3 electrons transfer during charge and discharge. H.-J. Dai et al [86] has developed a rechargeable Al-ion battery using Al as anode, three-dimensional graphite-foam as cathode, and $AlCl_3$/[EMIm]Cl as electrolyte, which delivers a capacity of 70 mAh/g and power density of 3000 W/kg (similar to capacitors) and energy density of 40 Wh/kg. As shown in Fig.3, during discharge, $AlCl_4^-$ ions deintercalate from graphite layers followed by $AlCl_4^-$ ions transporting through the electrolyte and reacting with the Al anode leading to the formation of $Al_2Cl_7^-$ and electron transfer in external circuit. During charge, an opposite process occurs. The reversible reactions in anode and cathode respectively are

Figure 3: Schematic of Al-ion battery using graphite cathode and $AlCl_3$/[EMIm]Cl ionic liquid electrolyte [86].

$$Al + 7AlCl_4^- \rightleftharpoons 4Al_2Cl_7^- + 3e^-, \tag{1.3}$$

and

$$C_n[AlCl_4] + e^- \rightleftharpoons C_n + AlCl_4^-. \tag{1.4}$$

Graphite has a layered hexagonal structure. Intra-layer carbon atoms are bounded with sp^2 hybridized C-C bonds while inter-layer carbon atoms are bounded with van der Waals interactions [87]. The large distance (3.35 Å) between inter-layers makes graphite being a suitable ion-hosting material. Depending on the species of intercalated ions, graphite intercalation compounds(GICs) can be classified as donor-type (e.g. Li^+, Na^+, K^+, etc) and acceptor-type (e.g. F^-, BF_4^-, Al_4^-, SO_4^-, etc) [88]. The ion intercalation into graphite is a staging process, where stage n-1 represents the number of inter-layers between two filled graphene layers [89]. The atomic structure and intercalation mechanism of $AlCl_4^-$ graphite component ($AlCl_4$-GIC) have been studied with DFT method. Pathak [90] studied the staging mechanism of $AlCl_4^-$ intercalation into bulk graphite using DFT and AIMD method. His calculations show that $AlCl_4^-$ intercalates into graphite from stage

4 to stage 1 with very small diffusion barrier (∼0.01 eV). The calculated voltage and gravimetric capacity of stage 1 and stage 4 are 2.3 V, 69.62 mAh/g and 2.01 V, 25.94 mAh/g, respectively. Lu [91] comprehensively studied the geometry of $AlCl_4^-$ in graphite, the intercalant density, the staging mechanism and the simulated XRD pattern of $AlCl_4$-GIC with DFT calculations. His study shows that $AlCl_4^-$ intercalates into graphite with a single-layer tetrahedron geometry. The most favorable stage of $AlCl_4$-GIC is stage 4 with a calculated capacity of 70 mAh/g. The peak positions of simulated XRD pattern for stage 4 are also in good agreement with the values in Ref.93. However, Han's [92] calculations with DFT show that the fully charged graphic cathode in AIB is at stage 3 with a doubly stacked intercalate structure and a capacity of 105 mAh/g. Nevertheless, a higher capacity of ∼100 mAh/g has been achieved recently by Dai's group [93] at low temperature (-40°C). Dai also carried out an the *in situ* XRD measurement to study the mechanism of $AlCl_4^-$ intercalation into graphite. In this thesis, group of Dai and our group performed a combined *in situ* XRD and simulation to uncover the staging mechanism of $AlCl_4$-GIC. We modelled and optimized the atomic structure of $AlCl_4$-GICs with different numbers of $AlCl_4^-$ molecular from stage 6 to stage 3. The maximum intercalation number of $AlCl_4^-$ molecular is chosen so that the corresponding calculated capacity is comparable with experimental value. XRD patterns are also simulated based on optimized structures. By comparing the peak positions of the simulated XRD patterns with those in the in situ XRD spectrum, a continuous intercalation mechanism from stage 6 to stage 3 has been proposed.

2 Method

2.1 The Schödinger Equation

Most of the interesting properties of battery materials can be obtained by solving the many-body Schödinger equations. The Schödinger equation under non-relativistic, time-independent condition is written as

$$\hat{H}\Psi(\mathbf{r}_i, \mathbf{R}_I) = E\Psi(\mathbf{r}_i, \mathbf{R}_I). \tag{2.1}$$

$\hat{H}$ is the Hamiltonian operator of a many-body system including m nuclei and n electrons. Ψ is the wave function which depends on electronic coordinates ($\mathbf{r}_i$) and nuclear coordinates ($\mathbf{R}_I$). E is the eigenvalue of Schödinger equation which gives the ground state energy of many-body system. $\hat{H}$ in atomic unit is written as

$$\hat{H} = \underbrace{-\frac{1}{2}\sum_{i=1}^{n}\nabla_i^2}_{\hat{T}_\mathrm{e}} \underbrace{-\frac{1}{2}\sum_{I=1}^{m}\nabla_I^2}_{\hat{T}_\mathrm{n}} + \underbrace{\sum_{i=1}^{n}\sum_{j>i}^{n}\frac{1}{r_{ij}}}_{\hat{V}_\mathrm{ee}} + \underbrace{\sum_{I=1}^{m}\sum_{J>I}^{m}\frac{Z_I Z_J}{R_{IJ}}}_{\hat{V}_\mathrm{nn}} \underbrace{-\sum_{i=1}^{n}\sum_{I=1}^{m}\frac{Z_I}{r_{iI}}}_{\hat{V}_\mathrm{en}}. \tag{2.2}$$

r_{ij}, r_{iI} and R_{IJ} represent the distance between electron i and j, electron i and nucleus I, nucleus I and J respectively. $\hat{H}$ consists of five terms:

(i) kinetic energy of electrons and nuclei (1^{st} and 2^{st} terms),

(ii) repulsive interaction between electrons (3^{rd} term),

(iii) repulsive interaction between nuclei (4^{th} terms),

(iv) attractive interaction between nuclei and electrons (5^{th} term).

The eigenvalue of Eq.(2.1), E_tot is correspondingly described as the sum of energies obtained by operating $\hat{H}$ on Ψ

$$E_\mathrm{tot} = T_\mathrm{e} + T_\mathrm{n} + V_\mathrm{ee} + V_\mathrm{nn} + V_\mathrm{en}, \tag{2.3}$$

Most of the materials of interest in science and engineering are many-body systems. To calculate the exact total energy as well as physical and chemical properties of a many-body system, the many-body Schödinger equation has to be solved exactly. The degree of freedom of many-body system is $3m + 3n$ and any influence interaction with a single particle by other electrons and nuclei has to be considered in this coupled system. The complexity of the many-body wave function Ψ dramatically increases with the size of many-body system. Due to this reason, Schödinger equation has been only exactly solved for a hydrogen atom which consists of only one electron. Thus, in practice, to solve the many-body problem, several approximations have to be applied.

2.2 The Born-Oppenheimer approximation

One of the most important approximations widely used for many-body systems is the Born-Oppenheimer Approximation (BOA) [94]. M. Born and J. R. Oppenheimer proposed this approximation based on the fact that the mass of nuclei is much larger (the mass of proton is around 1800 times of electrons) than that electrons and therefore the movement of nuclei is much slower compared to that of electrons in the many-body system. It is thus reasonable if we assume that electrons can instantaneously follow the movement of nuclei. Based on this approximation, the overall wave function Ψ can be split into the product of electronic ψ_{e} and nuclear wave function ψ_{n}

$$\Psi_i(\mathbf{r}_i, \mathbf{R}_I) = \psi_{\mathrm{e}}(\mathbf{r}_i, \mathbf{R}_I)\psi_{\mathrm{n}}(\mathbf{R}_I), \tag{2.4}$$

where $\psi_{\mathrm{e}}(\mathbf{r}_i, \mathbf{R}_I)$ and $\psi_{\mathrm{n}}(\mathbf{R}_I)$ are electronic and nuclear wave functions respectively. Since the nuclei are treated as 'static', the coordinates of nuclei $\mathbf{R}_I$ are parameters instead of variables. The Schödinger equation can be also separated into the electronic and nuclear parts

$$\underbrace{(-\frac{1}{2}\sum_{i=1}^{n}\nabla_i^2 - \sum_{i=1}^{n}\sum_{I=1}^{m}\frac{Z_I}{r_{iI}} + \sum_{i=1}^{n}\sum_{j>i}^{n}\frac{1}{r_{ij}})}_{\hat{H}_{\mathrm{e}}}\psi_{\mathrm{e}}(\mathbf{r}_i, \mathbf{R}_I) = E_{\mathrm{e}}\psi_{\mathrm{e}}(\mathbf{r}_i, \mathbf{R}_I), \tag{2.5}$$

$$(-\frac{1}{2}\sum_{I=1}^{m}\nabla_I^2 + \sum_{I=1}^{m}\sum_{J>I}^{m}\frac{Z_I Z_J}{R_{IJ}} + E_{\mathrm{e}}(\mathbf{R}_I))\psi_{\mathrm{n}}(\mathbf{R}_I) = E_{\mathrm{tot}}\psi_{\mathrm{n}}(\mathbf{R}_I). \tag{2.6}$$

E_{e} is the total energy of electronic part. After the electronic Schödinger equation (2.5) being solved, the total energy of many-body system is just the sum of E_{e} and a constant for a fixed nuclear coordinate

$$E_{\mathrm{tot}} = E_{\mathrm{e}} + E_{\mathrm{n}}. \tag{2.7}$$

Within BOA, the degree of freedom of many-body system is reduced to $3n$ and the complexity of the overall wave function is remarkably reduced. The error introduced by BOA has been proved to be very small, especially when the nuclei is much heavier than electrons.

Solving a many-electron problem is still difficult in practical computations. To further simplify the problem, many attempts have been made by theoreticians. Among them, two *ab initio* methods are the Hartree-Fock (HF) method and density functional theory (DFT). The former is based on the wave function and the latter is based on the electron density. All the calculations in my thesis are carried out using DFT. Therefore DFT will

be discussed in more details. A short summary of the HF method will be given first to understand the difference between these two methods.

2.3 The Hartree-Fock Approximation

The HF approximation [95] was initiated by D. R. Hartree in 1928 and improved by V. A. Fock in 1930. The basis of this approximation is to split the overall wave function of n-electron system as an antisymmetric product of n one-electron orthonormal spin-orbitals (Slater Determinant). The coulomb and exchange interaction between n independent electrons are represented by an average potential. To further simplify the calculations, Roothaan [96] proposed to construct the HF spin orbitals with a linear combination of a set of basis functions. Solving Schödinger equation with the HF approximation is realized by an iterative process. The minimum energy of many-electron system can be reached by iteratively solving the spin orbitals and Hamiltonian. In the term of average potential, exchange interaction which originates from the Pauli's exclusion principle has been exactly calculated. However, the correlation interaction between electrons has been completely ignored. This leads to an always overestimated total energy of the many-electron system. The correlation interaction can be included by using post HF method, such as the Møller-Plesset perturbation theory (MP2, MP4, etc) [97, 98], configuration interaction (CI, CISD) [99] and coupled cluster (CC, CCSD, etc) [100].

2.4 Density Functional Theory

With using the HF method, even under the BOA, the wave function of a system consisting of n electrons is a $4n$ ($3n$ spatial and n spin) variable functional. This limits the practical application of the HF method to only small-number-electron systems. In comparison to wave function-based methods, density-based methods are more practical for studying large-number-electrons systems. A widely used density-based method is the DFT. The origin of DFT is dated back to the Thomas-Fermi (TF) model which will be reviewed briefly in the following.

2.4.1 Thomas-Fermi-Dirac Model

In 1927, L. H. Thomas [101] and E. Fermi [102] proposed using electron density $\rho(\mathbf{r})$ to describe the Hamiltonian and energy of many-body systems. The definition of $\rho(\mathbf{r})$ is the

probability of finding one electron with arbitrary spin in the volume element $d\mathbf{r}_1$

$$\rho(\mathbf{r}_1) = n \int \cdots \int |\Psi(\mathbf{r}_1\sigma_1, \mathbf{r}_2\sigma_2, \cdots \mathbf{r}_n\sigma_n)|^2 d\sigma_1 d(\mathbf{r}_2\sigma_2) \cdots d(\mathbf{r}_n\sigma_n), \tag{2.8}$$

where $\mathbf{r}_1$, $\mathbf{r}_2$, $\cdots$, $\mathbf{r}_n$ are the spatial coordinates of electrons. σ_1, σ_2, $\cdots$, σ_n are the spins of electrons. $\rho(\mathbf{r}_1)$ is a function of three-dimensional spatial coordinates x, y, and z. The density integrates to the number of electrons n

$$\int \rho(\mathbf{r}) d\mathbf{r} = n. \tag{2.9}$$

The TF model calculates the kinetic energy of system under a homogeneous electron gas with constant electron density. The interaction between nuclei and electrons as well as between electrons are treated in a classical ways. The exchange and correlation interaction are completely ignored. The total energy functional of TF model is formulated as

$$E[\rho] = \frac{3}{10}(3\pi^2)^{\frac{2}{3}} \int d^3r \rho^{5/3}(\mathbf{r}) - Z \int \frac{\rho(\mathbf{r})}{\mathbf{r}} d\mathbf{r} + \frac{1}{2} \int d^3r_i d^3r_j \frac{\rho(\mathbf{r}_i)\rho(\mathbf{r}_j)}{r_{ij}}, \tag{2.10}$$

where the three terms in the right side are the kinetic energy, classical attractive electronic energy and classical repulsive electronic energy respectively.

In 1930, TF model was improved by P. A. M. Dirac [103] with introducing an electron density dependent exchange interaction term additionally

$$E_X = -\frac{3}{4}(\frac{3}{\pi})^{\frac{1}{3}} \int d^3r \rho^{4/3}(\mathbf{r}). \tag{2.11}$$

Although the TF model and TF-Dirac model are not successful in practical applications, they are the starting point of DFT leading to the development of density-based theory. After this early attempt, DFT was gradually developed and became one of the most important tools in study of materials using quantum mechanics. DFT has broad applications in battery material science to calculate, understand, and predict electronchemistry properties of electrode materials on the atomic level. In comparison to the Post HF method, DFT is computationally less expensive. The currently-used DFT method is based on the Hohnberg-Kohn Theorems. Furthermore, the Kohn-Sham equation developed in 1965 has initiated the practical application of DFT and spreads widely in nowadays.

2.4.2 Hohnberg-Kohn Theorems

The Hohenberg-Kohn theorems were introduced by P. Hohenberg and W. Kohn in 1964 [104]. The theorems include two main statements:

(1) For systems with non-degenerate ground state, the external potential $V_{\text{ext}}(\mathbf{r})$ (potential energy of interaction between electron i and the nuclei) is a unique functional of the ground state electron density $\rho(\mathbf{r})$. The Hamiltonian of system is written as

$$\hat{H} = \hat{T} + \hat{V}_{\text{ee}} + \hat{V}_{\text{ext}}. \tag{2.12}$$

The Hamiltonian $\hat{H}$, the ground state wave function Ψ and total energy of the ground state E can be also determined uniquely by $\rho(\mathbf{r})$. This relation can be simply descried as

$$\rho \;\Rightarrow\; V_{\text{ext}} \;\Rightarrow\; \hat{H} \;\Rightarrow\; \Psi \;\Rightarrow\; E \tag{2.13}$$

E of a particular system is written as

$$E(\rho) = \int \rho(\mathbf{r}) V_{\text{ext}} d\mathbf{r} + \underbrace{T(\rho) + V_{ee}(\rho)}_{F_{\text{HK}}(\rho)}, \tag{2.14}$$

where $F_{\text{HK}}(\rho)$ is called the Hohenberg-Kohn functional. The explicit form of $F_{\text{HK}}(\rho)$ is unknown. $V_{\text{ee}}(\rho)$ can be written as the sum of two different parts

$$V_{\text{ee}}(\rho) = \underbrace{\frac{1}{2}\int\int \frac{\rho(\mathbf{r}_i)\rho(\mathbf{r}_j)}{r_{ij}}}_{J(\rho)} + E_{\text{ncl}}(\rho). \tag{2.15}$$

J(ρ) is the coulomb repulsion between electrons. $E_{\text{ncl}}(\rho)$ is a non-classical term, including electronic self-interaction correlation, exchange and coulomb correlation.

(2) For all assumed electron density $\rho_v(\mathbf{r})$ which satisfies

$$\rho_v(\mathbf{r}) \geqslant 0, \int \rho_v(\mathbf{r}) d\mathbf{r} = n, \tag{2.16}$$

if and only if $\rho_v(\mathbf{r})$ equals to the true ground state electron density $\rho_0(\mathbf{r})$ of the system, the energy functional $E_v(\rho)$ equals to the exact ground state energy E_0 of the system

$$E(\rho_v) \geqslant E(\rho_0) = E_0. \tag{2.17}$$

The second theorem is an application of variational principle. Although the relation between E and $\rho(\mathbf{r})$ has been formulated as in Eq.(2.14), the explicit form of F_{HK} keeps unknown. To turn these theorems to practical calculations, approximations are needed to describe F_{HK}. In 1965, W. Kohn and L. J. Sham [105,106] proposed a relatively accurate way to approximate F_{HK}. The Kohn-sham (KS) approach is one of the most important approachs in DFT applications.

2.4.3 The Kohn-Sham Approach

In the KS approach, W. Kohn and L. J. Sham modeled a fictitious non-interacting system which posses the same electron density $\rho_0(\mathbf{r})$ as the ground state of a real many-electron system. The kinetic energy T(ρ) in Eq.(2.14) is then decomposed into two terms:

(1) The kinetic energy of the fictitious non-interacting system

$$T_{\mathrm{s}} = -\frac{1}{2}\sum_{i=1}^{n} < \varphi_i|\nabla_i^2|\varphi_i >, \tag{2.18}$$

where φ_i is the wave function of one-electron system, constructed by a linear combination of basis functions.

(2) The difference between kinetic energy of the real system T_0 and the fictitious non-interacting system

$$\Delta T = T_0 - T_{\mathrm{s}}. \tag{2.19}$$

F_{HK} is then rewritten as

$$F_{\mathrm{HK}}[\rho] = T_{\mathrm{s}} + J(\rho) + \underbrace{(T_0 - T_s) + E_{\mathrm{ncl}}(\rho)}_{E_{\mathrm{XC}}}, \tag{2.20}$$

where E_{XC} is the exchange-correlation energy including the kinetic energy difference between the real system and the fictitious non-interacting system as well as the non-classical energy term. The energy functional of the fictitious system is described as

$$E(\rho) = T_{\mathrm{s}}(\rho) + \int \rho(\mathbf{r}) V_{\mathrm{ext}} d\mathbf{r} + J(\rho) + E_{\mathrm{XC}}(\rho). \tag{2.21}$$

The first three terms on the right side of Eq.(2.21) are easy to be expressed with electron density ρ, while the form of E_{XC} is not known exactly. Although the contribution of E_{XC} to the ground state energy of many-electron system is relatively small, a good approximation of E_{XC} is the key of an accurate DFT result. Finding a suitable approximation of E_{XC} is also the main challenge of DFT development.

The Hamiltonian of KS system is

$$\begin{aligned} \hat{F}_{\mathrm{KS}} =& \hat{T}_{\mathrm{KS}} + \hat{V}_{\mathrm{coul}} + \hat{V}_{\mathrm{ext}} + \hat{V}_{\mathrm{XC}} \\ =& -\frac{1}{2}\nabla^2 + \underbrace{\int \frac{\rho(\mathbf{r}_j)}{r_{ij}} d\mathbf{r}_j - \sum_{I}^{m} \frac{Z_I}{r_{iI}} + \frac{\delta E_{\mathrm{XC}}[\rho(\mathbf{r})]}{\delta \rho(\mathbf{r})}}_{\hat{V}_{\mathrm{eff}}}. \end{aligned} \tag{2.22}$$

The first three terms are the kinetic operator, classical coulomb potential and external potential respectively. $\hat{V}_{\mathrm{XC}}$ is the exchange-correlation potential which is the functional derivative of E_{XC}.

The single particle KS equation is formulated as

$$(-\frac{1}{2}\nabla^2 + \hat{V}_{\mathrm{eff}})\varphi_i^{\mathrm{KS}} = \varepsilon_i \varphi_i^{\mathrm{KS}}, \tag{2.23}$$

where φ_i^{KS} is the KS orbital and ε_i is the orbital energy.

Solving the KS equation starts from modelling a fictitious n non-interacting system constructed with a set of orthonormal KS orbitals $\varphi_i^{\mathrm{KS}}(\mathbf{r}_1, \mathbf{r}_2, \cdots, \mathbf{r}_n)$. The initial electron density is expressed with φ_i^{KS} as

$$\rho^{\mathrm{KS}}(\mathbf{r}) = \sum_{i=1}^{occ} |\varphi_i^{\mathrm{KS}}(\mathbf{r})|^2, \tag{2.24}$$

where the summation runs over all occupied orbitals. By solving Eq.(2.23) and (2.24) iteratively until the electron density $\rho(\mathbf{r})$ is converged within required accuracy, the minimized total energy E of the many-electron system can be obtained from Eq.(2.21).

If and only if the form of E_{XC} is known exactly, a real ground-state energy E_0 of the many-electron system can be obtained from DFT calculation. Since this is not the case, approximation of E_{XC} have to be applied in practical DFT calculations. Various methods have been proposed to approximate E_{XC}. Some most commonly used E_{XC} approximations are summarized in following.

2.5 Exchange Correlation functional

2.5.1 Local (Spin) Density Approximation—L(S)DA

A simple way to approximate E_{XC} with electron density is to treat the electron density ρ of an inhomogeneous system locally as a uniform electron gas. This approximation is called the local density approximation (LDA) [107]. The model of LDA is constructed as: an infinitive number of interacting electrons move in an infinitive-size box where positive charge are uniformly distributed. The total charge of the system is neutral. Within this model, E_{XC} is formulated as

$$E_{\mathrm{XC}}^{\mathrm{LDA}}(\rho) = \int \rho(\mathbf{r}) \varepsilon_{\mathrm{XC}}(\rho(\mathbf{r})) d\mathbf{r}, \tag{2.25}$$

where $\varepsilon_{\mathrm{XC}}$ is the exchange-correlation energy per electron for a homogeneous gas at $\mathbf{r}$ with a density of $\rho(\mathbf{r})$. $\varepsilon_{\mathrm{XC}}$ can be written as the sum of two components: the exchange energy ε_{X} and the correlation energy ε_{C}

$$\varepsilon_{\mathrm{XC}}(\rho) = \varepsilon_{\mathrm{X}}(\rho) + \varepsilon_{\mathrm{C}}(\rho). \tag{2.26}$$

The formula of ε_{X} is clear based on Dirac's work on the uniform electron gas

$$\varepsilon_X = -\frac{3}{4}\sqrt[3]{\frac{3\rho(\mathbf{r})}{\pi}}. \tag{2.27}$$

ε_{C} is calculated with highly accurate Monte-Carlo simulations under homogeneous electron gas circumstance. There is no explicit form for ε_{C}. One example of the accurate expressions of ε_{C} is $\varepsilon_{\mathrm{C}}^{\mathrm{VWN}}(\rho)$ developed by Vosko, Wilk and Nusair in 1980 [108]. If the spin (α or β) of electrons is considered, Eq.(2.25) becomes

$$E_{\mathrm{XC}}^{\mathrm{LSDA}}(\rho) = \int \rho(\mathbf{r})\varepsilon_{\mathrm{XC}}(\rho_\alpha(\mathbf{r}), \rho_\beta(\mathbf{r}))d\mathbf{r}. \tag{2.28}$$

This is the local spin density approximation (LSDA) [109]. LSDA is more suitable for unrestricted systems, which consist different number of α electrons and β electrons.
Within L(S)DA, although ρ of the system is treated in a simple way, the spherically averaged distance between electrons has been well approximated. On one hand the well-approximated distance distribution has made the exchange-correlation hole (h_{XC}) possess of similar properties as a real inhomogeneous system since h_{XC} is a function of $\mathbf{r}$, resulting in relatively good results for not only close-homogeneous systems but also inhomogeneous systems. On the other hand the spherically averaged distance underestimates the bond length between atoms, leading to underestimated lattice constant and overestimated bond energy and cohesive energy. To improve the accuracy of properties like lattice constant and bond energy in DFT calculations, other approximations have been developed for E_{XC}.

2.5.2 The Generalized Gradient Approximation—GGA

GGA approximation [110] considered the gradient of the density $\nabla\rho$ in addition to the density ρ. If the spin of electrons are also considered, E_{XC} is formulated as

$$E_{\mathrm{XC}}^{\mathrm{GGA}}(\rho) = \int \rho(\mathbf{r})\varepsilon_{XC}(\rho_\alpha(\mathbf{r}), \rho_\beta(\mathbf{r}), \nabla\rho_\alpha(\mathbf{r}), \nabla\rho_\beta(\mathbf{r}))d\mathbf{r}. \tag{2.29}$$

Both $E_{\mathrm{X}}^{\mathrm{GGA}}$ and $E_{\mathrm{C}}^{\mathrm{GGA}}$ are not explicitly formulated. Different approximations have been initiated for their description such as the PW91 exchange-correlation functional proposed

by Burke, Perdew and Wang in 1991 [111], P86 exchange-correlation functional developed by Perdew in 1986 [112], and the one being used in my thesis, PBE exchange-correlation functional by Perdew, Burke and Ernzerhof in 1996 [113].

The exchange component of PBE functional is written as

$$E_{\mathrm{X}}^{\mathrm{PBE}}(\rho) = \int \rho(\mathbf{r})\varepsilon_{\mathrm{X}}^{\mathrm{unit}}(\mathbf{r})F_X(s_\sigma)d\mathbf{r}, \tag{2.30}$$

where $\varepsilon_{\mathrm{X}}^{\mathrm{unit}}(\mathbf{r})$ has the same formula as Eq.(2.27). F_{X} function is written as

$$F_X = 1 + k - \frac{k}{1 + \mu s^2/k}, \tag{2.31}$$

where $k = 0.804$ and $\mu \approx 0.21951$. s is a dimensionless density gradient with the formula

$$s = \frac{|\nabla\rho|}{2(3\pi^2\rho)^{1/3}\rho}. \tag{2.32}$$

The correlation component of PBE is much more complicated. More variables and parameters are introduced

$$E_{\mathrm{C}}^{\mathrm{GGA}}(\rho) = \int d\mathbf{r}\rho(\mathbf{r})[\varepsilon_C(r_s,\zeta) + H(r_s,\zeta,t)], \tag{2.33}$$

with

$$H(r_s,\zeta,t)] = \gamma ln(1 + \frac{\beta t^2}{\gamma}[\frac{1 + At^2}{1 + At^2 + A^2t^4}]), \tag{2.34}$$

and

$$\gamma \approx 0.031; \beta \approx 0.066; A = \frac{\beta}{\gamma}\frac{1}{e^{\frac{-\varepsilon_c^{unit}}{\gamma}} - 1}; t = \frac{|\nabla\rho|}{2((\frac{4(3\pi^2\rho)^{1/3}}{\pi})^{1/2})\rho}. \tag{2.35}$$

r_s is the local Seitz radius. $\zeta = (\rho_\alpha - \rho_\beta)/n$ is the relative spin polarization and t is another dimensionless density gradient. The ground state properties calculated from GGA have been improved compared with L(S)DA, especially for the lattice constant and total energy of systems. GGA is widely used in recent DFT calculations for solid-state system.

Despite the success of L(S)DA and GGA functionals in DFT calculations, they fail in predicting correct behavior of strongly correlated systems such as Mott insulators like 3d-transition-metal oxides. This failure is due to the insufficient description of L(S)DA or GGA for the orbital-polarization effects caused by the localization of 3d electrons in transition-metal oxides. An underestimated band gap usually obtained by L(S)DA or GGA. These strongly correlated systems can be well described by multi-band Hubbard model. The method based on Hubbard model is the so-called DFT+U method.

2.6 DFT+U

The Hubbard model is proposed to describe d or f electrons in transition metals. The Hubbard Hamiltonian is defined as [114]

$$\hat{H} = -t \sum_{\langle i,j\rangle,\sigma} c^{\dagger}_{i,\sigma} c_{j,\sigma} + U \sum_{i=1} n_{i\uparrow} n_{i\downarrow}. \tag{2.36}$$

The first term is the kinetic energy term, describing the hopping of electron between two nearest-neighbouring sites in the lattice. t is the energy scale which governs this hopping behavior. $\langle i,j\rangle$ is the summation over two adjacent lattice sites. $c^{\dagger}_{i,\sigma}$ and $c_{i,\sigma}$ are the creation and annihilation operator, respectively which creates or destroys an electron with spin σ on site i. The second term is the on-site Coulomb repulsion term. An energy U is added when one site is doubly occupied (one electron with spin up and another one with spin down). $n_{i\uparrow}$ and $n_{i\downarrow}$ are the number of electrons with spin up and spin down respectively. For systems such as metals which are dominated by single-particle terms of the energy (t$\gg$U), the first term of Eq.(2.36) can be well described by DFT method. However, for Mott insulators such as $LiNiO_2$ the second term of Eq.(2.36) is needed. DFT+U is a simple approach to describe the on-site Coulomb repulsion by adding a U correction to DFT method. The general formulation of energy functional in DFT+U is written as

$$E_{\mathrm{DFT+U}}[\rho^{\sigma}, \{n^{\sigma}\}] = E_{\mathrm{DFT}}[\rho^{\sigma}] + E_{\mathrm{Hub}}[\{n^{\sigma}\}] - E_{\mathrm{dc}}[\{n^{\sigma}\}]. \tag{2.37}$$

Here, $\{n^{\sigma}\}$ is the density matrix. $E_{\mathrm{Hub}}[\{n^{\sigma}\}]$ is the energy term derived from the Hubbard Hamiltonian. $E_{\mathrm{dc}}[\{n^{\sigma}\}]$ is added to avoid the double-counting of the electronic interactions which are already partially included in the DFT energy. A. Liechtenstein et al [115] proposed basis set independent formula of E_{Hub} and E_{dc}, which is also the most complete formula of DFT+U. However, in our thesis, a simpler expression of E_{Hub} proposed by Dudarev, S. L. [116] has been used.

2.7 van der Waals interaction and D3 dispersion

The van der Waals (vdWs) interaction is a non-directional intermolecular force between atoms and molecules of any type. Different from ionic or covalent interaction, vdWs interaction does not form any chemical bonds. Although vdWs is much weaker compared with other interactions, it is necessary in explaining some properties of materials. Two of the

most prototypical examples are the existence of liquid and solid state of noble gases and the formation of well-developed layers in graphite. vdWs originates from the temporary fluctuating dipole in molecule. The temporary dipole induce dipoles in all other molecules. Standard DFT calculations fail to describe correct properties of systems which held together by vdWs interactions such as layered structures like graphite due to the problem in describing long-range dispersion forces. In the study of layered structures, extra expression for vdWs interaction has to be added to standard DFT calculations. Some of commonly used approaches are such as the DFT-D$^{(1-3)}$ correction method series [117,118], the non-local van der Waals functional vdW-DF [119,120], the dispersion-corrected atom-centered potentials DCACPs method [121] and the 'pure'density functional (DF) [122]. In this thesis, the DFT-D3(BJ) method (BJ is the abbreviation of Becke-Jonson damping) has been used to model graphite and the $AlCl_4^-$ intercalated graphite compounds.
The DFT-D3 correction method treats vdWs as a damped atom-pair wise potential. The energy functional of DFT-D3 approximation is written as

$$E_{\mathrm{DFT-D3}} = E_{\mathrm{DFT}} - E_{\mathrm{disp}}, \tag{2.38}$$

where E_{disp} is the dispersion correction energy. With BJ damping, E_{disp} is formulated as [123]

$$E_{\mathrm{disp}}^{\mathrm{D3(BJ)}} = \frac{1}{2}\sum_{A\neq B} s_6 \frac{c_6^{\mathrm{AB}}}{r_{\mathrm{AB}}^6 + (a_1 R_0^{\mathrm{AB}} + a_2)} + s_8 \frac{c_8^{\mathrm{AB}}}{r_{\mathrm{AB}}^8 + (a_1 R_0^{\mathrm{AB}} + a_2)}. \tag{2.39}$$

c_6^{AB} and c_8^{AB} are the averaged dispersion coefficients of 6^{th}- and 8^{th}-order dispersion. r_{AB} is the internuclear distance. R_0^{AB} is the cut off radius of atom pair AB which specifies the distance region where the absolute value of dispersion energy exponentially decreases. s_6 and s_8 are the global scaling factors. a_1 and a_2 are adjustable parameters. The value of a_1, a_2, s_6 and s_8 are exchange-correlation functional dependent. In our calculations where PBE functional has been used, we consider the value of a_1, a_2, s_6 and s_8 to be 0.4289, 4.4407, 1.0000 and 0.7875, respectively [123].

2.8 Basis function

To solve the KS equation (2.23) and (2.24) computationally efficiently, the KS orbitals are represented as linear combinations of electronic basis functions $\eta_\chi(\mathbf{r})$

$$\varphi_i^{\mathrm{KS}}(\mathbf{r}) = \sum_{\chi=1}^{N_{\mathrm{basis}}} c_{\chi i}\eta_\chi(\mathbf{r}), \tag{2.40}$$

where N_{basis} and $c_{\chi i}$ are the number and coefficient of the basis function, respectively. In principle, a complete set of basis functions must be used to represent the exact KS orbital. However, to balance the accuracy and speed of the calculation, a certain finite number of basis functions are used in practical calculations. Two different types of basis functions, namely atomic orbital and plane waves, have been employed in this thesis. The overview of these basis functions will be presented briefly in this section.

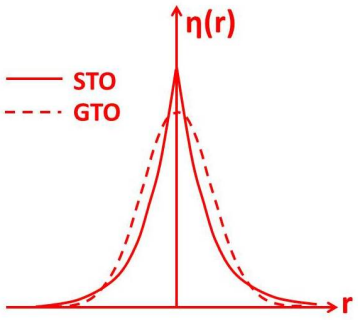

Figure 4: An example of the STO and GTO function.

Atomic orbital (AO) basis function. There are two common types of AOs have been used by researchers. (i) Slater-type-orbitals (STOs) [124] are the simplistic basis function used due to their similarity with the eigenfunction of hydrogen atom. A typical STO in spherical coordinate (r, θ, ϕ) is written as

$$\eta^{\text{STO}} = N r^{n-1} Y_{lm}(\theta, \phi) e^{-\zeta r}, \tag{2.41}$$

where N is a normalization factor. n, l, and m are the principal quantum number, the angular momentum quantum number and its z component, respectively. ζ is the orbital exponent determining the spatial expansion of the wave function. Y_{lm} is a spherical harmonic for the angular part of the function. Although the STO shows correct cusp behavior near the nucleus and correct exponential decay far from the nucleus, numerical methods have to be used for the three- and four-center integrals calculation which are very computational consuming. Another widely used basis function in density- or wave function- based method is the Gaussian-type-orbital (GTO) [125]. The general formula of GTO in Cartesian coordination (x, y, and z) is written as

$$\eta^{\text{GTO}} = N x^i y^j z^k e^{-\zeta r^2}, \tag{2.42}$$

where $l = i + j + k$. Although more GTOs are required to achieve a certain accuracy compared with STOs, the usage of GTOs is computationally more efficient due to the existence of very efficient algorithms for calculating the four-center integrals. GTOs are popular as basis functions in electronic structure calculations. Nevertheless, GTOs have problem in representing the proper behavior near the nucleus and fall off too rapidly far

from the nucleus. An example of the STO and the GTO function is shown in Fig.4. Contracted Gaussian function (CGF) combines the superiority of GTO and STO. A certain number of primitive GTOs are linearly combined such that the CGF can perform similar as a single STO function. The formula of CGF is written as

$$\eta^{\mathrm{CGF}} = \sum_{a}^{A} d_a \eta_a^{\mathrm{GTO}}, \tag{2.43}$$

where A is the number of GTOs used to create a CGF basis function. d_a is a contraction coefficient. d_a is determined so that the CGF performs as a STO function. In this thesis, CGFs have been used with SeqQuest code.

Plane wave (PW) basis function is a non-localize basis function which expands over the whole space. It is an exponential function with a general form

$$\eta^{\mathrm{PW}} = e^{i\mathbf{k}\cdot\mathbf{r}}. \tag{2.44}$$

Here, $\mathbf{k}$ is a wave vector and $\mathbf{r}$ is a position vector in space. PWs are widely used in solid-state system with periodical boundaries. Relatively large number of PWs are needed to achieve an acceptable accuracy. In practical calculations, the number of PWs can be determined by the value of energy cutoff E_{cutoff} according to

$$E_{\mathrm{cutoff}} \geqslant \frac{\hbar^2}{2m}|\mathbf{G}|^2. \tag{2.45}$$

$\mathbf{G}$ is a lattice vector in reciprocal space. In this thesis, PWs basis functions have been used with VASP code.

2.9 Periodic systems

All the systems studied in this thesis are periodic systems which possess of periodically arranged atoms. In principle, an infinite number of wave functions and basis sets are needed to solve KS equation for a periodic system, which is not possible in practical DFT calculations. To model a periodic system in a simple way, the smallest possible unit cell possessing the same atomic arrangement as the periodic system is chosen. For example, to model a 3-dimensional structure such as **bulk**, a primitive unit cell (i.e. Bravais lattice)

or at most few primitive unit cells is considered. To model a 2-dimensional structure such as **surface** (e.g. thin film or graphene), the periodicity along the surface is kept, while the periodicity perpendicular to the surface is broken by adding a vacuum region (Fig.5). Here, the surface is represented by periodically repeated supercell slab model. To avoid the interaction between neighbouring slabs, the vacuum region should be wide enough. Two surfaces are exposed in the supercell slab model. The thickness of the slab should be also large enough to avoid the interaction between these two exposed surfaces.

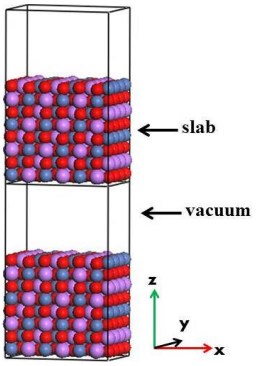

Figure 5: Schematic representation of a supercell slab model.

2.9.1 Bloch Theorem

The electronic wave function of a periodic system can be written as the multiplication of a periodical function $u_{n,\mathbf{k}}(\mathbf{r})$ and a plane wave

$$\psi_{n,\mathbf{k}}(\mathbf{r}) = u_{n,\mathbf{k}}(\mathbf{r})e^{i\mathbf{k}\cdot\mathbf{r}}, \tag{2.46}$$

where $u_{n,\mathbf{k}}(\mathbf{r})$ has the same periodicity as the lattice of the system. n is the *band* index. $e^{i\mathbf{k}\cdot\mathbf{r}}$ is a plane wave (Eq. 2.44). $u_{n,\mathbf{k}}(\mathbf{r})$ can be also expanded by a set of plane waves

$$u_{n,\mathbf{k}}(\mathbf{r}) = \sum_{G} c_{n,\mathbf{k}}(\mathbf{G})e^{i\mathbf{G}\cdot\mathbf{r}}. \tag{2.47}$$

In periodic systems, the Fourier transform of Bravais lattice is called the reciprocal lattice. A lattice vector in the real space $\mathbf{L}$ and its reciprocal space $\mathbf{G}$ fulfil the following condition

$$\mathbf{G}\cdot\mathbf{L} = 2\pi\nu, \tag{2.48}$$

where ν is an integer. Inserting Eq.(2.47) into Eq.(2.46) gives us

$$\psi_{n,\mathbf{k}}(\mathbf{r}) = \sum_{G} c_{n,\mathbf{k}}e^{i(\mathbf{k}+\mathbf{G})\cdot\mathbf{r}}. \tag{2.49}$$

This equation is called the Bloch theorem [126]. On the basis of Bloch theorem, the single-particle wave functions ψ_i in KS equations can be expanded by a set of plane waves. With this approach, the DFT calculations will be computationally simplified.

2.9.2 Sampling of Brillouin Zone

The first Brillouin Zone (BZ) is the primitive cell of crystal in reciprocal space. To calculate the properties of a periodic system such as the density of state and total energy, integration over the first BZ in reciprocal space is needed

$$f = \frac{1}{\Omega_{\mathrm{BZ}}} \int f(\mathbf{k}) d\mathbf{k}, \tag{2.50}$$

where Ω_{BZ} is the volume of the first BZ. Mathematically, this integration is replaced with a discrete sampling of $\mathbf{k}$ space

$$\frac{1}{\Omega_{\mathrm{BZ}}} \int f(\mathbf{k}) d\mathbf{k} \Rightarrow \sum_k w_k f(\mathbf{k}), \tag{2.51}$$

where w_k is weighting factors of $\mathbf{k}$-points. In a practical calculation, a finite number of $\mathbf{k}$-points is enough to achieve the accuracy required. The $\mathbf{k}$-points can be constructed with different methods. In this thesis, the Monkhorst and Pack $\mathbf{k}$-point meshes method [127] has been applied, in which $\mathbf{k}$-points distribute homogeneously through the BZ and along x, y, z axes in the reciprocal space.

2.10 Pseudopotentials

The all-electron wave function consists of two parts: (1) the core wave function ψ_{c} corresponding to the core electrons which occupy the innermost shells and do not often participate in the formation of chemical bonding, (2) the valance wave function ψ_{v} corresponding to the valance electrons which occupy the outermost shells and participate in the formation of chemical bonding. The strong interaction between nuclei and core electrons causes large oscillations of ψ_{v} since ψ_{v} must be orthogonal to ψ_{c}. Therefore, a large number of basis sets (i.e. PWs) is needed to expand the electronic wave function. Most of the physical and chemical properties of materials are mainly determined by the valance electrons. To reduce the computational cost, the core electrons can be considered to be frozen [128]. H. Hellmann [129] proposed that the potential of core electrons (determined by a cut-off radius r_{c}) can be replaced by an effective potential while the potential of valence electrons (outside radius r_{c}) is still the same as the real potential. This is called the **pseudopotential** approximation [130]. Simultaneously, a pseudo wave function

is constructed with a smooth (nodeless) core part $\psi_{\rm c}$ and an accurate all-electron-like valance part $\psi_{\rm v}$. Schematic representations of $\psi^{\rm ps}$, $V^{\rm ps}$, $\psi^{\rm ae}$, and $V^{\rm ae}$ are shown in Fig.6. The pseudopotential approximation reduces the number of PWs required and thereby reduces the expense of DFT calculations. Most commonly used pseudopotentials are the norm-conserving pseudopotentials (NCPPs) [132, 133], projector augmented wave (PAW) [134,135], and the ultrasoft pseudopotentials (USPPs) [136]. In this thesis, NCPPs are used in calculations with SeQqust Code and PAWs are implemented in calculations with VASP code.

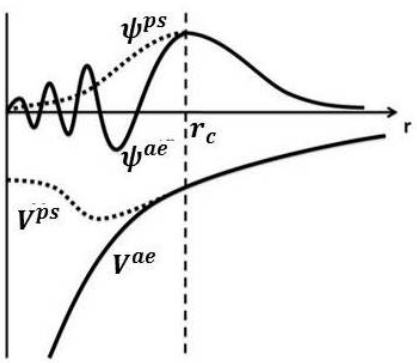

Figure 6: Schematic representations of $\psi^{\rm ps}$, $V^{\rm ps}$, $\psi^{\rm ae}$, and $V^{\rm ae}$ [131].

2.10.1 Norm conserving pseudopotential (NCPP)

NCPP was proposed by D. R. Hamann et al [132]. For a chosen reference atomic configuration, NCPP must fulfil the following conditions:

(i) The orbital energy of electron under pseudopotential and all-electron potential are the same $\varepsilon_l^{\rm ps} = \varepsilon_l^{\rm ae}$.

(ii) $\psi_l^{\rm ps}(r)$ is nodeless for $r < r_{\rm c}$.

(iii) $\psi_l^{\rm ps}(r) = \psi_l^{\rm ae}(r)$ for $r > r_{\rm c}$.

(iv) Norm of pseudo wave function equals to norm of all-electron wave function inside radius $r_{\rm c}$

$$\int_{r<r_c} |\psi_l^{\rm ps}(r)|^2 r^2 dr = \int_{r<r_c} |\psi_l^{\rm ae}(r)|^2 r^2 dr.$$

(v) The logarithmic derivative of pseudo and all-electron wave function agrees at r_c

$$\frac{\psi'^{\rm ps}}{\psi^{\rm ps}} = \frac{\psi'^{\rm ae}}{\psi^{\rm ae}}.$$

NCPP is one of the most commonly used pseudopotentials in DFT calculations. The advantage of NCPP is that its transferability among different atomic configurations are relatively high. The disadvantage is that in many systems such as the transition metals, a large number of PWs are needed to expand the wave function, which requires a high computational expense.

2.10.2 Projector augmented wave (PAW)

PAW [134] is another commonly used pseudopotential in DFT calculations. In this section, **bra-ket notation** is used to simplify the description. A linear transformation operator $\hat{T}$ is defined so that the true all-electron wave function $|\psi\rangle$ can be obtained from an auxiliary smooth PS wave function $|\tilde{\psi}\rangle$ ($\sim$ is used for smooth functions)

$$|\psi\rangle = \hat{T}|\tilde{\psi}\rangle, \tag{2.52}$$

with

$$\hat{T} = 1 + \sum_R \hat{T}_R. \tag{2.53}$$

Here, $|\psi\rangle$ is a KS single-particle wave function. An augmentation sphere $|\mathbf{r} - \mathbf{R}| < r_c$ is constructed around each atom. $\mathbf{R}$ is the atom position. $\hat{T}_R$ acts only in this augmentation sphere. Out of this augmentation sphere, $|\psi\rangle_O = |\tilde{\psi}\rangle_O$. Inside this sphere, the auxiliary smooth PS wave function $|\tilde{\psi}\rangle_I$ is expanded by a set of PS partial waves $|\tilde{\phi}_i\rangle$

$$|\tilde{\psi}\rangle_I = \sum_i |\tilde{\phi}_i\rangle c_i, \quad |\mathbf{r} - \mathbf{R}| < r_c. \tag{2.54}$$

c_i is the expansion coefficient. The index i is referred to the atom position $\mathbf{R}$ and the angular momentum quantum number l, m. The corresponding all-electron wave function within the sphere can be also written as the expansion of a set of AE partial waves $|\phi_i\rangle$

$$|\psi\rangle_I = \hat{T}|\tilde{\psi}\rangle = \sum_i |\phi_i\rangle c_i, \quad |\mathbf{r} - \mathbf{R}| < r_c. \tag{2.55}$$

Since the operator $\hat{T}$ is linear, c_i can be written as an inner product with a set of projector functions $\langle\tilde{p}_i|$

$$c_i = \langle\tilde{p}_i|\tilde{\psi}\rangle, \tag{2.56}$$

where $\langle\tilde{p}_i|$ fulfils the condition $\langle\tilde{p}_i|\tilde{\phi}_j\rangle = \delta_{\mathrm{ij}}$. Afterwards, the all-electron wave function $|\psi\rangle$ can be expressed by $|\tilde{\psi}\rangle$, $|\phi_i\rangle$, and $|\tilde{\phi}_i\rangle$ as

$$\begin{aligned} |\psi\rangle =& |\tilde{\psi}\rangle - \sum_i |\tilde{\phi}_i\rangle c_i + \sum_i |\phi_i\rangle c_i \\ =& |\tilde{\psi}\rangle + \sum_i (|\phi_i\rangle - |\tilde{\phi}_i\rangle)\langle\tilde{p}_i|\tilde{\psi}\rangle, \end{aligned} \tag{2.57}$$

with

$$\hat{T} = 1 + \sum_i (|\phi_i\rangle - |\tilde{\phi}_i\rangle)\langle\tilde{p}_i|. \tag{2.58}$$

In Eq.(2.57), $|\psi\rangle$ has been separated into an auxiliary smooth function part which can be represented on coarse Fourier- or real space grids and a rapid oscillation contribution part (only in certain small areas of space). PAW is an accurate and efficient pseudopotential to calculate the electronic structures in DFT calculations.

2.11 Thermodynamics of defects

The Gibbs free energy G of a system at a constant temperature and pressure is written as

$$G = E_{\text{tot}} + \underbrace{(E_{\text{ZPE}} - TS_{\text{vib}})}_{F_{\text{vib}}} - TS_{\text{conf}} + PV. \tag{2.59}$$

E_{tot} is the total energy of the system at a steady state. F_{vib} is the vibrational free energy. F_{vib} was neglected in our calculations and the following description. E_{ZPE} is the zero-point energy. S_{vib} and S_{conf} are the vibrational and configurational entropy respectively. P and V are the pressure and the volume of crystal respectively. The contribution of $P\Delta V$ term is also negligible in a solid state system. The Gibbs formation energy ΔG of defect in crystal at a constant temperature and pressure is thus written as

$$\Delta G = \Delta E - T\Delta S_{\text{conf}}. \tag{2.60}$$

$\Delta E = E^p_{\text{tot}} - E^d_{\text{tot}}$ is the change of internal energy. E^p_{tot}, E^d_{tot} are the total energy of perfect and defective crystal, which both can be obtained directly from the DFT calculations. Therefore, at a constant temperature, ΔG is determined only by the value of ΔE and ΔS_{conf}. The creation of defect in a stable crystal costs some energy, which means ΔE is positive. The change of entropy due to the formation of defects in crystal is calculate by

$$\Delta S_{\text{conf}} = k_{\text{B}} lnW = k_{\text{B}} ln(\frac{N!}{(N-n_{\text{s}})!\, n_{\text{s}}!}), \tag{2.61}$$

where k_{B} is the Boltzmann constant. n_{s} and N are the number of defects and the number of possible sites in crystal, respectively. W represents the number of ways to randomly distribute n_{s} defects in N possible sites of crystal. Inserting Eq.(2.61) to Eq.(2.60) and using Stirling's approximation [137], ΔG is rewritten as

$$\Delta G = n_s \Delta E_s - k_{\text{B}} T\{N\text{ln}N - (N-n_s)\text{ln}(N-n_s) - n_s\text{ln}n_s\}, \tag{2.62}$$

where ΔE_{s} is the energy required to form one mole of defects. At equilibrium, the change of ΔG respects to the change of defect numbers Δn_{s} is zero, $\frac{d\Delta G}{d\Delta n_{\text{s}}} = 0$. Therefore at any

temperature, the equilibrium population of defects in crystal is

$$n_{\mathrm{s}} \approx N e^{\frac{-\Delta H_{\mathrm{s}}}{k_B T}}. \tag{2.63}$$

The presence of defects plays key role in electronic and ionic conductivity [138–140]. Theoretical study of defects in crystal is therefore important and helpful for researchers to understand and improve the properties (such as the capacity) of battery materials. Point defects are the most common type of defects in crystal and also the type studied in this thesis. Point defects can be classified as two types:

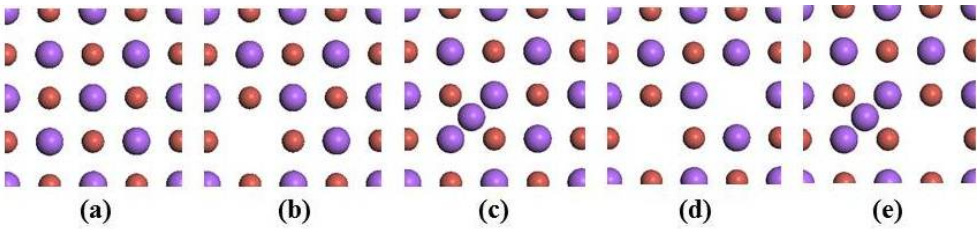

Figure 7: Atomic arrangement of (a) pristine (b) vacancy defect (c) interstitial defect (d) Schottky defect and (e) Frenkel defect.

(I) **intrinsic defects**

Vacancy defect forms when one atom is removed from the perfect crystal (Fig.7b).

Interstitial defect creates when one extra atom is added to a position where no atom ought to be appeared (Fig.7c).

Schottky defect consists of paired vacancies in the cation and anion sub-lattices (e.g. Na vacancy and Cl vacancy form a Schottky defect in NaCl)(Fig.7d).

Frenkel defect consists of a pair of interstitial and vacancy defects (e.g. a Na interstitial defect and a Na vacancy defect form a Frenkel defect)(Fig.7e).

Formation of vacancy or interstitial defects can be compensated by electrons or holes. However, the neutrality of crystal is kept with the formation of Schottky and Frenkel defect.

(II) **Extrinsic defect**

Dopant defect forms when a low concentration of extrinsic elements replace intrinsic elements in crystal. Effect of dopant on the structure and performance of battery materials is very important for researchers and has been widely studied. In this thesis, the effect of Zr dopant on $LiNiO_2$ will be studied.

2.11.1 Chemistry of defects

In this thesis, the supercell approach has been used to model the formation of defects in crystal. The formation energy of defects (i) with different charge states (q) in supercell is calculated as [141]

$$\Delta E_{\mathrm{f}}^{i,q} = \underbrace{E_{\mathrm{tot}}^{i,q} - E_{\mathrm{tot}}^{\mathrm{p}} + n_i\mu_i}_{\Delta E_{\mathrm{f}}^{i,0}} + q(\epsilon_{\mathrm{F}} + \epsilon_{\mathrm{VBM}}) + \underbrace{q\Delta V_{q/0} + E_{\mathrm{corr}}}_{\Delta E}, \tag{2.64}$$

where $E_{\mathrm{tot}}^{i,q}$ and E_{tot}^{p} are the total energy of defective and pristine supercell respectively. n_i and μ_i are the number (+/- for vacancy/interstitial defect) and chemical potential of each defect element. The sum of the first three terms are the formation energy $\Delta E_{\mathrm{f}}^{i,0}$ of neutral defects in the supercell. When the defects are charged, the chemical potential of the electrons (4^{th} term in Eq.(2.64)) has to be introduced to compensate the charge difference between the defective and neutral supercell. ϵ_{F} is the Fermi level referred to the bulk valance-band maximum (VBM) energy (ϵ_{VBM}). $\Delta V_{q/0}$ is the alignment of electrostatic potential in defective supercell with that in pristine supercell. E_{corr} is the correction for electrostatic interactions of defect with its periodic images and the compensating background. To calculate ΔE, in this thesis, the **FNV** approach proposed by C. Freysoldt, J. Neugebauer and C. G. Van de Walle [142, 143] has been used.

The main drawback of the supercell approach is the finite-size effect. In the supercell model, instead of an isolated defect, a periodic array of defects are created. The large density and periodic arrangement of the defects in supercell result in artificial interactions between the charge and their images. Moreover, for a charged supercell a compensating background has to be included. Otherwise the electrostatic energy will diverge because of the infinite number of electron-electron repulsion between charged defects. Usually, a homogeneous neutralizing background is chosen. The interaction between defect and the compensating background should be also corrected in the formation energy calculation. The interactions E_{corr} between defect and its images and the compensating background decrease asymptotically as the size of the supercell L increases. Electrostatic potential alignment $\Delta V_{q/0}$ can be calculated by the electrostatic potential at where is far from the defect when the unit cell is large enough. However, very large unit cell are needed because of the slow q/r (r is the distance between defect and any point in the supercell) decay of the defect's coulomb potential. Therefore, alternative approach is needed to calculate E_{corr} and $\Delta V_{q/0}$. One of the effective ways is the **FNV** approach. Within **FNV**, a model

defect charge distribution which has the same defect charge as the supercell is built. The simplest model is the point-charge model. Within **FNV**, the correction is written as

$$E_{\mathrm{corr}}^{\mathrm{FNV}} = E_{\mathrm{lat}} - q\Delta V_{q/0}, \tag{2.65}$$

where E_{lat} is the lattice energy of the model defect charge distribution. In the point-charge model case, E_{lat} equals to $\frac{q^2\alpha}{2\varepsilon L}$, where α is the Madelung constant and ε is the dielectric constant. The potential alignment $\Delta V_{q/0}$ is calculated by subtracting the potential of the model charge from the potential difference between charge and neutral supercell

$$\Delta V_{q/0} = (V_q^{\mathrm{DFT}} - V_0^{\mathrm{DFT}})|_{\mathrm{far}} - V^{\mathrm{model}}|_{\mathrm{far}}, \tag{2.66}$$

where V_q^{DFT} and V_0^{DFT} are the potential of charge and neutral defective supercell, respectively. V^{model} is the potential of the model charge. The subscript means all the potentials are far from the defect. It is worth to mention that the value of $E_{\mathrm{corr}}^{\mathrm{FNV}}$ is independent of the form of the model defect charge distribution as long as the defect charge is well localized in the model.

To calculate the Fermi level, we considered the charge neutrality requirement of the supercell

$$\underbrace{\int_{\mathrm{CBM}}^{\infty} D(\epsilon) f(\epsilon, \epsilon_F) d\epsilon}_{n_{\mathrm{e}}} - \underbrace{\int_{-\infty}^{\mathrm{VBM}} D(\epsilon)[1 - f(\epsilon, \epsilon_F)] d\epsilon}_{n_{\mathrm{h}}} = \underbrace{\sum_i q_i n_i^0 e^{(-\frac{\Delta E_f^{i,q}}{k_B T})}}_{n_i}. \tag{2.67}$$

Here, $D(\epsilon)$ is the calculated density of state of the pristine and $f(\epsilon, \epsilon_F)$ is the Fermi-Dirac distribution [144, 145] with the formula

$$f(\epsilon, \epsilon_F) = \{1 + e^{(\frac{\epsilon - \epsilon_F}{k_{\mathrm{B}} T})}\}^{-1}. \tag{2.68}$$

In Eq.(2.67) n_{e}, n_{h} and n_i are the concentration of electrons, holes and defects of type i, respectively. n_i^0 is the maximum possible concentration of defects of type i per unit volume. q_i is the charge state of defect type i. $\Delta E_{\mathrm{f}}^{i,q}$ and ϵ_{F} are obtained by iteratively solving Eq. (2.64) and (2.67).

2.12 Ion transport

Ion transport is a key process in energy storages determining the performance of battery materials. In a defective crystal, ion or defect may transport generally via three different

mechanisms [146]. (i) **Vacancy hopping** mechanism. The nearby ion hops to the existing vacant site and fills it, leaving its original site empty (e.g. Na vacancy transports via A⟶B in Fig.8(a)). (ii) **Interstitial hopping** mechanism. The interstitial atom hops to the next nearest interstitial site in each hopping process (e.g. Na interstitial atom transports via C⟶D in Fig.8(b)). (iii) **"Knock-off"** mechanism [147]. Interstitial atom

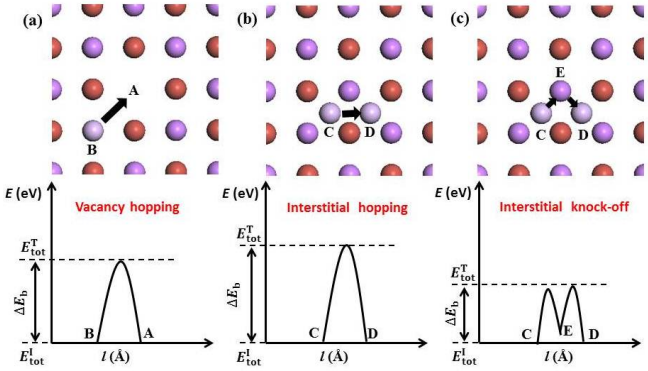

Figure 8: Schematic and diffusion barrier of (a) vacancy hopping mechanism, (b) interstitial hopping mechanism and (c) interstitial "Knock-off" mechanism.

continuously displaces the atom at a neighbouring lattice site instead of direct hopping through the empty space between two adjacent interstitial sites (e.g. Na interstitial atom transports via C⟶E⟶D in Fig.8(c)). The energy needed for a successful diffusion (jump) of an ion or defect is called the diffusion barrier ΔE_{b}, which is calculated by the difference between the the total energy of the transition state $E^{\mathrm{T}}_{\mathrm{tot}}$ and the total energy of the initial state $E^{\mathrm{I}}_{\mathrm{tot}}$ (see Fig.8). Different mechanisms may happen in one defective crystal. The mechanism which gives the lowest activation energy E_{a} is the determining mechanism. Ionic diffusivity [148] D is one of the important factors to describe the ion or defect migration. In 1-dimensional diffusion process, D can be estimated by

$$D \approx \frac{1}{2}\nu l^2 e^{-\frac{\Delta E_{\mathrm{b}}}{k_{\mathrm{B}}T}}, \tag{2.69}$$

where l, T and ν are the distance between initial and final site (see Fig.8), the temperature and the diffuse frequency of ion or defect, respectively. In this thesis, ν is calculated using harmonic transition state theory approximation

$$\nu = \frac{\Pi^{3N}\nu_i^{\mathrm{G}}}{\Pi^{3N-1}\nu_i^{\mathrm{T}}}, \tag{2.70}$$

where ν_i^{G} and ν_i^{T} are real vibrational frequencies of the ground state and the transition state respectively. The maximum (1-dimensional) diffusion length L in a solid crystal for

a given time t is calculated by

$$L \approx (2Dt)^{\frac{1}{2}}. \tag{2.71}$$

In this thesis, the diffusion barrier and diffusivity of Li^+ ion diffusion in bulk Li_xTiO_2-B ($0<x\leq1.25$) have been calculated by Eq.(2.69). The maximum diffusion length of Li^+ ion diffusion in bulk Li_xTiO_2-B with different Li^+ ion concentration have been also calculated using Eq. (2.71) to find the effect of kinetic on the capacity of Li_xTiO_2-B materials.

2.12.1 Nudged elastic band (NEB) method

As mentioned above, ΔE_b is an important factor to calculate the diffusivity of ions or defects. Several different pathways may exist between the initial and final site. However, only the one with the lowest energy barrier (minimum energy path-MEP) is the rate determining pathway. One commonly used method to find the MEP and calculate the diffusion barrier is called the **NEB** method [149]. Within the NEB method, a set of images (4 to 20) is constructed between the initial and final states. Adjacent images are connected by an elastic band like a spring to make sure the successive of the pathway. Elastic force introduced by the spring and the true force due to the potential energy of the system will be applied to each image. There might be several local maximum points along the MEP, which are called the saddle points. Only the one with highest energy is defined to be ΔE_b of ion or defect diffusion. Therefore it is very important to find out the real highest saddle point in NEB calculations. The more images constructed between the initial and final states, the easier to find the real highest saddle point. The NEB method has been implemented in many DFT-codes so far. In this thesis, the NEB method was used to calculate the diffusion barrier of Li^+ ion hoping in bulk Li_xTiO_2-B with SeqQuest and VASP and the diffusion barrier of Li^+ vacancy migration in rock-salt Li based LiX (X = I, Br, and Cl) materials with VASP.

2.13 Modelling of XRD patterns

2.13.1 Fundamental principle of XRD measurement

XRD is a valuable technique to (i) measure the distance between layers and rows of atoms, (ii) identify atomic structure, and (iii) provide information on unit cell dimensions.

When doing the measurement, monochromatic x-ray beam goes through the crystal sample. The x-ray waves interfere with one another when they leave the crystal (the scattering of x-ray) due to the effect of atomic planes in crystal. Although most of the waves are cancelled out with one another because of the destructive interference, some of the waves will produce constructive interference in some special directions. This phenomenon is called the x-ray diffraction. The production of constructive interference must satisfy the Bragg's Law [150]

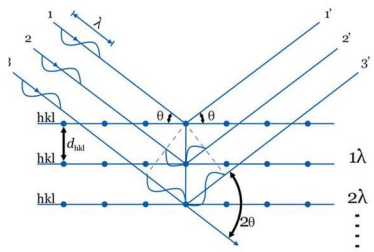

Figure 9: Schematic of x-ray diffraction across planes in crystal.

$$2d_{hkl}\sin\theta = c_1\lambda. \tag{2.72}$$

Here, d_{hkl} is the distance between paralleled (hkl) plane in crystal. θ is the incident angle and 2θ is the diffraction angle. c_1 is any integer and λ is the wavelength of x-ray. λ is determined by the target element such as Cu, Fe, Mo and Cr which is used to produce x-ray beam. The schematic of x-ray diffraction across planes in crystal is shown in Fig.9. Experimentally by scanning the crystal sample through a range of 2θ angles, all possible diffraction planes of the lattice can be recognised based on the peak positions in XRD pattern. The averaged distance d_{hkl} of each plane can be also calculated with Eq.(2.72).

2.13.2 XRD simulation with geometry of crystal

The XRD pattern can be simulated if the geometry of crystal (atomic coordinates and lattice parameters) is known already. With a given λ value and the known $d_{(hkl)}$ spacing value, all the peak positions (2θ) respected to plane (hkl) can be simulated by changing the value of c_1. The structure factor F for a reflection (hkl) in crystal is formulated as

$$F(hkl) = \sum_{j=1}^{n} g_j[f_{0j}(hkl) + f' + if'' + f_{\mathrm{NT}}]T_j(hkl)e^{i2\pi(hx_j+ky_j+lz_j)}, \tag{2.73}$$

where n is the number of atoms in the unit cell. x_j, y_j, and z_j are the fractional coordination of atom j and g_j is the occupation. f_{0j} is the atomic form factor. f' and f'' are the real and imaginary part of the dispersion correction, respectively which are calculated by linear interpolation of theoretically calculated form factors in energy ranges of E = 1–10 eV and E = 0.4–1.0 MeV [151, 152]. f_{NT} is the nuclear Thompson scattering [153]. T_j is

the Debye-Waller factor. The coherent atomic scattering factor f_0 is a function of $\sin\theta/\lambda$

$$f_0(sin\theta/\lambda) = \sum_{i=1}^{N} a_i e^{(bi\frac{sin^2\theta}{\lambda^2})} + c_2. \tag{2.74}$$

The a_i, b_i and c_2 parameters with N=5 used in VESTA is obtained from the table in [154]. These parameters can be used in a range of $0<\sin\theta/\lambda<6$. In this thesis, the lattice parameters and d_{hkl} spacing between graphene layers of graphite and $AlCl_4$-graphite component are calculated with DFT method and the XRD patterns for optimized structures are simulated with VESTA tool based on the structure factor. The target element is set to be Cu, and the wave length of the x-ray are 1.540 and 1.544 Å. Since the atomic scattering factor used in VESTA is specific for free atoms, the simulated XRD pattern may have some discrepancy compared to experimental XRD pattern.

3 Results and publications

3.1 Contributions in the Publications

In the first publication **A1**, I am the first author and Dr. Kaghazchi is the corresponding author. The literature review was done by me and the idea was created by Dr. Kaghazchi. I am responsible for modelling all the atomic structures, finding the diffusion pathways, performing the DFT calculations and summarizing the data. Dr. Kaghazchi helped me to analyse the data. In writing the manuscript, all the figures and tables were prepared by me and the writing task was mainly performed by Dr. Kaghazchi and a small part by me.

In the second publication **A2**, I am the first author and Dr. Kaghazchi is the corresponding author. The idea was also created by Dr. Kaghazchi based on reviewing of literature by me. I calculated the formation energy of all possible defects and Fermi energy of LiX (X=I, Br, and Cl) components as a function of Li chemical potential using DFT method combined with thermodynamic considerations. I also calculated the diffusion barriers and activation energies of Li vacancy transport in LiX. All the figures of the manuscript were prepared by me. Dr. Kaghazhi helped me to analyse the data and he wrote the manuscript.

The third publication **A3** was a joint project between Dr. Kaghazchi's group at FU Berlin and Prof. Dai's group at Stanford University. The idea was proposed by Prof. Dai and all the experimental work were performed by his group. I studied the staging mechanism of $AlCl_4^-$ intercalation into graphite with DFT+D3 calculations and simulated the XRD patterns for the optimized structures. Dr. Kaghazchi gave me some important suggestions and helped me to analyse the data. The comparison between D2 and D3 correction (Table S1), the structures of $AlCl_4^-$ graphite components from stage 6 to stage 3 (Figure 3 and Figure S4) as well as the simulated XRD patterns and peak positions (Figure 3 and Table S2) were all prepared by me. The text of theory part was written by Dr. Kaghazchi. The experimental part of the manuscript was written by Prof. Dai.

The fourth publication **A4** was a joint project between Dr. Kaghazchi's group at FU Berlin and Prof. Sun's group at Hanyang University. I calculated the percentage of Li-Ni interchange in non-doped $LiNiO_2$, the concentration of Zr dopant in $LiNiO_2$, and the charge compensation mechanism of $LiNiO_2$ after Zr doping using DFT+U method. The

effect of Zr dopant on the cation ordering (Li-Ni interchange ordering) and Li vacancy formation energy were also studied by me. Dr. Kaghazchi helped me in analysing the data. The atomic structures of non-doped and doped $LiNiO_2$ (Figure 6 and Figure S3, and Figure S4), the lattice parameters of non-doped and doped $LiNiO_2$ (Figure 7), and the Li vacancy formation energies of non-doped and doped $LiNiO_2$ (Table 1) were all prepared by me. The theory part of the manuscript was written by Dr. Kaghazchi and a small part by me. The experimental part of the manuscript was written by Prof. Sun.

3.2 Publication A1

"Li-Content Dependence of Li Diffusivity in TiO_2-B"

Qian Zhang and Payam Kaghazchi

J. Phys. Chem. C, 120(2016), pp. 22163-22168

DOI: 10.1021/acs.jpcc.6b06319

URL: `https://pubs.acs.org/doi/abs/10.1021/acs.jpcc.6b06319`

3.3 Publication A2

"Strong Dependence of Ion Transport on the Electronegativity of the Constituting Atoms in Ionic Crystals"
published as: "Dependence of Ion Transport on the Electronegativity of the Constituting Atoms in Ionic Crystals"

Qian Zhang and Payam Kaghazchi
ChemPhysChem, 18(2017), pp. 965-969

DOI: 10.1002/cphc.201601208
URL: `https://doi.org/10.1002/cphc.201601208`

3.4 Publication A3

"An operando X-ray diffraction study of chloroaluminate anion-graphite intercalation in aluminum batteries"

Chun-Jern Pan, Chunze Yuan, Guanzhou Zhu, Qian Zhang Chen-Jui Huang, Meng-Chang Lin, Michael Angell, Bing-Joe Hwang, Payam Kaghazchi, and Hongjie Dai
PNAS, 115(2018), pp. 5670-5675

DOI: 10.1073/pnas.1803576115
URL: `https://doi.org/10.1073/pnas.1803576115`

3.5 Publication A4

"Cation Ordering of Zr-Doped $LiNiO_2$ Cathode for Lithium-Ion Batteries"

Chong S. Yoon, Min-Jae Choi, Do-Wook Jun, Qian Zhang, Payam Kaghazchi, Kwang-Ho Kim, and Yang-Kook Sun

Chem. Mater., 30(2018), pp. 1808-1814

DOI: 10.1021/acs.chemmater.8b00619

URL: `https://pubs.acs.org/doi/abs/10.1021/acs.chemmater.8b00619`

4 Summary

In this thesis, we studied the insertion/extraction and transport of ions as well as the effect of dopant on the atomic structure and Li vacancy formation in some selected electrode materials by using DFT calculations combined with thermodynamic and kinetic considerations.

In the publication **A1**, we studied the Li^+ ion insertion and transport in Li_xTiO_2-B anode from thermodynamic and kinetic points of view and found that the latter factor (kinetics) controls the capacity of this system. Our study may also explain the reason of limited capacities for bulk TiO_2-B achieved in experimental labs. Li_xTiO_2-B with different x values (low-, intermediate-, intermediate high-, and high-concentration) with 8 different occupation configurations and 18 different pathways have been studied using DFT-PBE and PBE-based NEB method. Diffusivities of Li transport at each concentration were also calculated and compared. In the low-concentration interstitial case ($x \leq 0.25$), Li inserts in the lowest-energy Li sites (sites in the O layer). Diffusion of Li is direction-dependent but it is not limited because of the low diffusion barrier. In the intermediate-concentration regime ($0.25 < x \leq 0.75$), Li inserts gradually into the four Li sites of TiO_2 layer and two Li sites of the O layer. A slightly higher diffusion barrier compared to the low-concentration interstitial case was found because of the repulsion between Li atoms in TiO_2 layers. In both low- and intermediate-concentration cases, Li migration is relatively fast and not kinetic limited. In the intermediate high-concentration interstitial case ($0.75 < x \leq 1.00$), the rest two Li sites in O layer are occupied. The structures remain stable after optimization. However, two times higher diffusion barrier and six orders of magnitude smaller diffusivity were found for Li diffusion compared to the intermediate-concentration case. In this case, the diffusion of Li in Li_xTiO_2-B is limited because of the strong repulsion between Li atoms in TiO_2 layer and O layer. In the high-concentration interstitial case ($1.00 < x \leq 1.25$), the Li sites in the center of channel are occupied. Although the structures are energetically favorable, Li transport along the channel is limited due to an extremely high diffusion barrier (2.03 eV) and thereby extremely low diffusivity (order of -36 magnitude). The lithiation of Li_xTiO_2-B is therefore kinetically very unfavorable. With all these results, we proposed that the capacity of TiO_2-B is mainly limited by the kinetic factor. At the end, to quantitatively show the relation between the particle size and the capacity of TiO_2-B, the maximum diffusion length of Li as a function of C-rate

(hC rate means that the battery is fully discharged in 1/h hour) was estimated. The maximum capacity evaluated for bulk ($r > 1$ μm) and nano-structured (1 μm $> r >$1 nm) TiO_2-B are 251 mAh/g and 335 mAh/g, respectively, which are in fair agreement with experimental values.

In the publication **A2**, we studied Li ion transport mechanism and activation energy E_a in Li-based binary components LiX (X=I, Br, and Cl) as a function of Li chemical potential (or operating voltage) using DFT-PBE method combined with thermodynamic and kinetic considerations. The relation between the value of E_a and the fundamental property (electronegativity) of element in LiX is also established. This study may also explain the reason for different reported E_a values by experimentalists. We firstly studied the thermodynamics of defects by calculating the defect formation energy (ΔE_f) of all possible defect types (neutral and charged) and the Fermi energy (ϵ_F) as a function of Li chemical potential (or voltage). In the high chemical potential (or low voltage) regime, the Schottky defect is found to be the most favorable defect in LiX. In this regime the number of electrons and the number of holes in LiX crystal are the same and negligible, which is characterized by the intrinsic regime. In the low chemical potential (or high voltage) regime, Li vacancy defect (V_{Li}^-) becomes the most favorable defect in LiX. In this regime, holes are created in the valence band maximum (VBM) because of the excitation of electrons from the VBM to defect states. The charge of holes is compensated by V_{Li}^-, which is characterized by the p-type regime. Moreover, the kinetics of defect was also studied by calculating the energy barrier ΔE_b of Li vacancy hopping in LiX. The value of ΔE_b increases with the increasing of stability (lower Gibbs energy of formation ΔG_f) of LiX. Afterwards, we calculated E_a by combing the thermodynamics and kinetics of defects. In the intrinsic regime, E_a is calculated by the sum of formation energy of Schottky pairs and the energy barrier of Li vacancy hopping. E_a does not change with the decreasing of Li chemical potential in the intrinsic regime and is the maximum value of E_a (E_a^{max}). In the p-type regime, E_a is calculated by the sum of the formation energy of Li vacancy and the diffusion barrier of Li vacancy hopping. E_a decreases with the decreasing of Li chemical potential in the p-type regime. The minimum value of E_a (E_a^{min}) is obtained at the lowest Li chemical potential. We found that with the decreasing of Li chemical potential, both the mechanism and activation energy of Li ion transport in LiX change. We also found that all the reported experimental values of E_a are in the range

between E_a^{max} and E_a^{min}. At the end, well-defined linear relation between activation energy (maximum and minimum) and ΔG_f of LiX is established. The slope of the fitted line of E_a^{max} to ΔG_f is found to be equal to the slope of the line fitted to the electronegativity of X^- as a function of ΔG_f. Therefore, the maximum activation energy of Li transport in LiX is quantitatively related to the electronegativity of X^-. A larger electronegativity value will lead to a higher activation energy of LiX.

In the publication **A3**, we performed a joint research with the group of Prof. H.-J. Dai at Stanford University. The staging mechanism of $AlCl_4^-$ intercalation into graphite has been studied using DFT-PBE method with the D3 dispersion to correctly represent the long-range interaction between graphene layers. The lattice constant of pristine graphite calculated with D3 was also in good agreement with experimental values. This work also reveals that stable $AlCl_4^-$/graphite intercalation occurs at stage 3 at low temperature (stage 3) [93] instead of stage 4 at room temperature [86]. The Rüdorff model was considered to model the atomic structure of $AlCl_4$-GICs from stage 6 to stage 3. Different number of intercalation $AlCl_4^-$ anions (1 to 4) in each intercalation layer (32 C atoms) of graphite have been considered. After the optimization, all the structures are stable. To be comparable with the experimental value ($\sim$ 100 mAh/g) reported by Dai's group [93], the number of intercalated $AlCl_4^-$ anions in each intercalation layer is considered to be 4 for all the stages. After optimization, the $AlCl_4^-$ anions in $AlCl_4$-GICs are single stacked with tetrahedral geometry. The gallery height of an anion intercalation layer in graphite is 9.49–9.54 Åfor stages 6 to 3. Then, the XRD patterns from small angle to large angle were simulated based on structural factors of the optimized structures. Furthermore, the peak positions are calculated based on the Bragg's law of diffraction. There are some small extra peaks in simulated XRD pattern compared with experimental XRD pattern due to the scattering from $AlCl_4^-$ anions. Besides these small extra peaks, the simulated peaks at the large-angle position ($> 5°$) are in good agreement with experimental results. However, the simulated peaks at the small-angle position ($\leqslant 5°$) have $\sim$10% discrepancies with experimental values. Moreover, the relative intensity of simulated peaks is different from that of the experimentally measured peaks, which may be due to the inaccurate scattering parameters for Al and Cl ions used in the XRD simulation. By comparing the peak positions of simulated and measured XRD patterns, the staging mechanism of $AlCl_4^-$ intercalation into graphite is found to be from stage 6 to stage 3 during the charge

process.

In the publication **A4**, we performed a joint research with the group of Prof. Y.-K. Sun at Hanyang University. We studied the percentage of Li-Ni interchange in non-doped $LiNiO_2$, the concentration of Zr dopant in $LiNiO_2$, and the charge compensation mechanism of $LiNiO_2$ after Zr doping as well as the effect of Zr dopant on the cation ordering (Ni distributes homogeneously in Li layer) and Li vacancy formation. DFT-PBE with U parameter is used in order to correct the on-site Coulomb interaction in the localized 3d electrons of Ni. To calculate the percentage of Li-Ni interchange in non-doped $LiNiO_2$, lattice constants of non-doped $LiNiO_2$ with different percentages of Li-Ni interchange were calculated. Both a and c parameters were found to decrease with the increase of interchange degree in $LiNiO_2$. To calculate the concentration of Zr doped in $LiNiO_2$, the lattice constants of ordered $[Li_{0.75}Ni_{0.25}]_{3a}[Ni_{0.75}Li_{0.25}]_{3b}O_2$ with different percentages of Zr dopant were calculated. We found that both a and c parameters increase with the increase of dopant concentration. By comparing these calculated lattice parameters with experimental values, the percentage of Li-Ni interchange in non-doped $LiNiO_2$ and the concentration of Zr dopant in $[Li_{0.75}Ni_{0.25}]_{3a}[Ni_{0.75}Li_{0.25}]_{3b}O_2$ were determined. To study the mechanism of charge compensation of $LiNiO_2$ after Zr doping, three different structures are considered. The charge of $LiNiO_2$ can be compensated by either changing the valence of Ni or forming three Li vacancies around each Zr. However, to achieve the high initial discharge capacity (90% of the theoretical capacity of $LiNiO_2$) reported by Sun, the charge of $LiNiO_2$ is more likely to be compensated by the self-valence change of Ni. To study the effect of Zr dopant on the cation ordering of $LiNiO_2$, the interchange energy per Li(Ni) of ordered $[Li_{0.75}Ni_{0.25}]_{3a}[Ni_{0.75}Li_{0.25}]_{3b}O_2$ without and with Zr and the total energy of 9 disordered (Ni distributes randomly in Li layer) $[Li_{0.75}Ni_{0.25}]_{3a}[Ni_{0.75}Li_{0.25}]_{3b}O_2$ structures with Zr dopant were calculated. We found that the interchange energy of Li(Ni) decreases after Zr doping. Furthermore, the total energy of ordered structure is lower compared to disordered structures. Therefore, Zr dopant promoted the cation mixing and cation ordering of $LiNiO_2$. Finally, to study the effect of Zr dopant on the Li vacancy formation of $LiNiO_2$, the Li vacancy formation energy of non-doped and Zr doped $LiNiO_2$ were calculated in low Li vacancy concentration case ($\leqslant$0.1875). Similar values of Li vacancy formation energy have been achieved for both cases, therefore Zr dopant does not change the Li vacancy formation energy of $LiNiO_2$.

Acknowledgement

I would like to express my sincere gratitude to my supervisor Dr. Payam Kaghazchi for his valuable guidance, scholarly inputs and consistent encouragement throughout my phD study. He introduced me to the world of quantum chemical modelling and taught me many fundamentals of theoretical chemistry and skills of chemical modelling.
My deep gratitude goes to Prof. Dr. Beate Paulus, who gave me enormous help during my doctor study, especially after knowing that I was pregnant.
Many thanks to Dr. Jean Christophe Tremblay, who helped me a lot to prepare for the administration exam. I am quite appreciative for Prof. Dr. Christina Roth and her colleagues, who gave me chances to learn from them. I am grateful for Mrs. Julija Djordjevic for her administrative work and for her help in applying for scholarship.
I further extend my private gratitude to Sara Panahian Jand, Liangyin Kuo, Ashkan Moradabadi and Pouya Partovi-Azar for their helpful suggestions related my research. To Xuefei Wen, Chunmei Liu and Kangli Wang, thank for making my life in Berlin exciting and fun.
I greatly appreciate the funding received towards my PhD study from China Scholarship Council (CSC). For computational resources, I thank Zentraleinrichtung für Datenverarbeitung (ZEDAT) at Freie Universität Berlin and the Hochleistungsrechenzentrum Nord (HLRN).
Last but not least, a very special word of thanks goes for my family. I would express a heartfelt thank for my parents, whose warm love and endless support are with me in whatever I pursue. More specially, I would like to thank my husband, the love of my life, Jie Liu, for his continued patience and encouragement.

Declaration of Authorship

I hereby confirm that I have authored this doctorate thesis independently and without use of others than the indicated sources. All passages which are literally or in general matter taken out of publications or other sources are cited as such.

Berlin, October 23, 2018

Qian Zhang

References

[1] S. Goriparti, E. Miele, F. D. Angelis, E. D. Fabrizio, R. P. Zaccaria, and C. Capiglia *J. Power Sources*, vol. 257, pp. 421–443, 2014.

[2] M. M. Kabir and D. E. Demirocak *Int. J. Energy Res.*, vol. 41, pp. 1963–1986, 2017.

[3] W. Li, B. Song, and A. Manthiram *Chem. Soc. Rev.*, vol. 46, pp. 3006–3059, 2017.

[4] K. Kreder and A. Manthiram *ACS Energy Lett.*, vol. 2, pp. 64–69, 2017.

[5] X. Li, M. Gu, S. Hu, R. Kennard, P. Yan, X. Chen, C. Wang, M. J. Sailor, J.-G. Zhang, and J. Liu *Nat. Commun.*, vol. 5, p. 4105, 2014.

[6] T. Zhao, Q. Wang, and P. Jena *ACS Energy Lett.*, vol. 1, pp. 202–208, 2016.

[7] S. Kim, S. Choi, K. Lee, and G. J. Yang *Phys.Chem.Chem.Phys.*, vol. 19, p. 4104, 2017.

[8] M. Xie, T. Hu, L. Yang, and Y. Zhou *RSC. Adv.*, vol. 6, pp. 63250–63255, 2016.

[9] X. F. Tang, G. W. Wen, Y. Zhang, D. Wang, and Y. Song *Appl. Surf. Sci.*, vol. 425, pp. 742–749, 2017.

[10] A. G. Dylla, P. H. Xiao, G. Henkelman, and K. J. Stevenson *Appl. Surf. Sci.*, vol. 425, pp. 2015–2019, 2012.

[11] B. B. Chen, S. Y. Chu, R. Cai, S. Y. Wei, R. Q. Hu, and J. Q. Zhou *Comp. Mater. Sci*, vol. 123, pp. 44–51, 2016.

[12] C. K. Chan, R. Ruffo, S. S. Hong, and Y. Cui *J. Power Sources*, vol. 189, pp. 1132–1140, 2009.

[13] Y. B. Liu, T. L. Ding, D. L. Shen, J. Dou, and M. D. Wei *J. Elec. Chem.*, vol. 804, pp. 87–91, 2017.

[14] J. Hu, F. Zhang, C. Z. Shao, B. Z. Li, Y. Li, and Y. G. Yang *Mater. Lett.*, vol. 210, pp. 363–365, 2018.

[15] A. Kraytsberg and Y. Ein-Eli *J. Power Sources*, vol. 196, pp. 886–893, 2011.

[16] X. Yao, Q. Dong, Q. Cheng, and D. Wang *Angew. Chem. Int. Ed.*, vol. 55, pp. 11344–11353, 2016.

[17] X. Ji, K. T. Lee, and L. F. Nazar *Nat. Mater.*, vol. 8, pp. 500–506, 2009.

[18] A. Manthiram, Y. Fu, and Y.-S. Su *Acc. Chem. Res.*, vol. 46, pp. 1125–1134, 2013.

[19] X. Ji and L. F. Nazar *J. Mater. Chem.*, vol. 20, pp. 9821–9826, 2010.

[20] C. Lai, X. P. Gao, B. Zhang, T. Y. Yan, and Z. Zhou *J. Phys. Chem. C*, vol. 113, pp. 4712–4716, 2009.

[21] D. Aurbach, E. Pollak, R. Elazari, G. Salitra, C. S. Kelley, and J. Affinito *J. Electrochem. Soc.*, vol. 156, pp. A694–A702, 2009.

[22] M. S. Reisch *Chemical and Engineering News*, vol. 95, pp. 19–21, 2017.

[23] Q. Li and N. J. Bjerrum *J. Power Sources*, vol. 110, pp. 1–10, 2002.

[24] N. Jayaprkash, S. K. Das, and L. A. Archer *Chem. Commun.*, vol. 47, pp. 12610–12612, 2011.

[25] A. V. der Ven, J. C. Thomas, Q. Xu, B. Swoboda, and D. Morgan *Phys. Rev. B*, vol. 78, p. 104306, 2008.

[26] E. A. Suslov, O. V. Bushkova, E. A. Sherstobitova, O. G. Reznitskikh, and A. N. Titov *Ion.*, vol. 22, pp. 503–514, 2016.

[27] G. Zhong, Y. Li, P. Yan, Z. Liu, M. Xie, and H. Lin *J. Phys. Chem. C*, vol. 114, pp. 3693–3700, 2010.

[28] M. Atanasov, J. Barras, L. Benco, and C. Daul *J. Am. Chem. Soc.*, vol. 122, pp. 4718–4728, 2000.

[29] J. Lee, A. Urban, X. Li, D. Su, G. Hautier, and G. Ceder *Science*, vol. 343, pp. 519–522, 2014.

[30] X. Feng, Y. Gao, L. Ben, Z. Yang, Z. Wang, and L. Chen *J. Power Sources*, vol. 317, pp. 74–80, 2016.

[31] H. Shiiba, M. Nakayama, and M. Nogami *Solid State Ion.*, vol. 181, pp. 994–1001, 2010.

[32] G. Xu, K. Zhong, J. M. Zhang, and Z. Huang *J. Appl. Phys.*, vol. 116, p. 063703, 2014.

[33] K. Tatsumi, Y. Sasano, S. Muto, T. Yoshida, T. Sasaki, K. Horibuchi, and Y. Ukyo *Phys. Rev. B*, vol. 78, p. 045108, 2008.

[34] F. Kong, R. C. Longo, M. S. Park, J. Yoon, D. H. Yeon, J. H. Park, and K. Cho *J. Mat. Chem. A*, vol. 3, pp. 8489–8500, 2015.

[35] C. M. Schauerman, M. J. Ganter, G. Gaustad, C. W. Babbitt, R. P. Raffaelle, and B. J. Landi *J. Mater. Chem.*, vol. 22, pp. 12008–12015, 2012.

[36] Y. Gu, F. Wu, and Y. Wang *Adv. Funct. Mater.*, vol. 23, pp. 893–899, 2013.

[37] M. Ge, J. Rong, X. Fang, and C. Zhou *Nano Lett.*, vol. 12, pp. 2318–2323, 2012.

[38] J. Yang, Y. Takeda, N. Imanishi, C. Capiglia, J. Y. Xie, and O. Yamamoto *Solid State Ionics*, vol. 152, pp. 125–129, 2002.

[39] I.-S. Hwang, J.-C. Kim, S.-D. Seo, S. Lee, J.-H. Lee, and D.-W. Kim *Chem. Commun.*, vol. 48, pp. 7061–7063, 2012.

[40] K. Zhuo, M.-G. Jeong, and C.-H. Chung *J. Power Sources*, vol. 244, pp. 601–605, 2013.

[41] Z. Chen, I. Belharouak, Y. K. Sun, and K. Amine *Adv. Funct. Mater.*, vol. 23, pp. 959–969, 2013.

[42] M. Fehse, M. B. Yahia, L. Monconduit, F. Lemoigno, M. L. Doublet, F. Fischer, C. Tessier, and L. Stievano *J. Phys. Chem. C*, vol. 118, pp. 27210–27218, 2014.

[43] Y. Q. Wang, L. Gu, Y. G. Guo, H. Li, X. Q. He, S. Tsukimoto, Y. Ikuhara, and L. J. Wan *J. Am. Chem. Soc.*, vol. 134, pp. 7874–7879, 2012.

[44] J. Wang, J. Polleux, J. Lim, and B. Dunn *J. Phys. Chem. C*, vol. 111, pp. 14925–14931, 2007.

[45] C. Jiang, I. Honma, T. Kudo, and H. Zhou *Electrochem. Solid-State Lett.*, vol. 10, pp. A127–A129, 2007.

[46] K. Hoshina, Y. Harada, H. Inagaki, and N. Takami *J. Electrochem. Soc.*, vol. 161, pp. A348–A354, 2014.

[47] J. M. Li, W. Wan, H. H. Zhou, J. J. Li, and D. S. Xu *Chem. Commun.*, vol. 47, pp. 3439–3441, 2011.

[48] A. Vittadini, M. Casarin, and A. Selloni *J. Phys. Chem. C. Lett.*, vol. 113, pp. 18973–18977, 2009.

[49] A. G. Dylla, G. Henkelman, and K. J. Stevenson *Acc. Chem. Res.*, vol. 46, pp. 1104–1112, 2013.

[50] S. H. Liu, H. P. Jia, L. Han, J. L. Wang, P. F. Gao, D. D. Xu, J. Yang, and S. N. Che *Adv. Mater.*, vol. 24, pp. 3201–3204, 2012.

[51] C. Arrouvel, S. C. Parker, and M. S. Islam *Chem. Mater.*, vol. 21, pp. 4778–4783, 2009.

[52] A. S. Dalton, A. A. Belak, and A. V. der Ven *Chem. Mater.*, vol. 24, pp. 1568–1574, 2012.

[53] R.-J. Chen, T.-L. Zhao, X.-X. Zhang, L. Li, and F. Wu *Nanoscale Horizons*, vol. 1, pp. 423–444, 2016.

[54] N. Nitta, F. X. Wu, J. T. Lee, and G. Yushin *Mater. Today*, vol. 18, pp. 252–264, 2015.

[55] Y.-X. Gu, D.-R. Chen, and X.-L. Jiao *J. Phys. Chem. B*, vol. 109, pp. 17901–17906, 2005.

[56] J. H. Shim, J. Lee, S. Y. Han, and S. H. Lee *Elec. Acta*, vol. 186, pp. 201–208, 2015.

[57] J. Cho *Angew. Chem.*, vol. 113, p. 3471, 2001.

[58] I. D. Scott *Nano Lett.*, vol. 11, p. 414, 2010.

[59] J. H. Shim, J. Lee, S. Y. Han, and S. H. Lee *Electrochim. Acta*, vol. 186, pp. 201–208, 2015.

[60] Y.-K. Sun, S.-T. Myung, B.-C. Park, J. Prakash, I. Belharouak, and K. Amine *Nat. Mater.*, vol. 8, pp. 320–324, 2009.

[61] B. Liu, B. Xu, M. S. Wu, and C. Y. Ouyang *J. Electrochem. Sci.*, vol. 11, pp. 432–445, 2016.

[62] H.-J. Noha, S. Youna, C. S. Yoonb, and Y.-K. Sun *J. Power Sources*, vol. 233, pp. 121–130, 2013.

[63] A. O. Kondrakov, A. Schmidt, J. Xu, H. Geβwein, R. Mönig, P. Hartmann, H. Sommer, T. Brezesinski, and J. Janek *J. Phys. Chem. C*, vol. 121, pp. 3286–3294, 2017.

[64] K. Min, S.-W. Seo, Y. Y. Song, H. S. Lee, and E. Cho *Phys. Chem. Chem. Phys*, vol. 19, pp. 1762–1769, 2017.

[65] E. Peled, D. Golodnitsky, C. Menachem, and D. Bar-Tow *J. Electrochem. Soc.*, vol. 145, p. 3482, 1998.

[66] E. Peled, D. Bar-Tow, A. Merson, A. Gladkich, L. Burstein, and D. Golodnitsky *J. Power Sources*, vol. 52, pp. 97–98, 2001.

[67] D. Aurbach, M. D. Levi, E. Levi, and A. Schechter *J. Phys. Chem. B*, vol. 101, p. 2195, 1997.

[68] A. Kominato, E. Yasukawa, N. Sato, T. Ijuuin, H. Asahina, and S. Mori *J. Power Sources*, vol. 68, p. 471, 1997.

[69] S. Shi, Y. Qi, H. Li, and J. L. G. Hector *J. Phys. Chem. C*, vol. 117, pp. 8579–8593, 2013.

[70] Q. Zhang, J. Pan, P. Lu, Z. Liu, M. W. Verbrugge, B. W. Sheldon, Y.-T. Cheng, Y. Qi, and X. Xiao *Nano Lett.*, vol. 16, pp. 2011–2016, 2016.

[71] Y. C. Chen, C. Y. Ouyang, L. J. Song, and Z. L. Sun *J. Phys. Chem. C*, vol. 115, pp. 7044–7049, 2011.

[72] A. Naji, J. Ghanbaja, P. Willmann, and D. Billaud *Electrochim. Acta*, vol. 45, pp. 1893–1899, 2000.

[73] G.-B. Li, S. Zhou, P. Wang, and J.-J. Zhao *RSC. Adv.*, vol. 5, pp. 107326–107332, 2015.

[74] J. S. G. Myrdal, D. Blanchard, D. Sveinbjörnsson, and T. Vegge *J. Phys. Chem. C*, vol. 117, pp. 9084–9091, 2013.

[75] L.-Z. Fan, X.-L. Wang, and F. Long *J. Power Sources*, vol. 189, pp. 775–778, 2009.

[76] Y. You and A. Manthiram *Adv. Energy Mater.*, vol. 8, p. 1701785, 2018.

[77] H. Ma, H. Chen, and G. Ceder *J. Electrochem. Soc.*, vol. 158, pp. A1307–A1312, 2011.

[78] M. M. Huie, D. C. Bock, E. S. Takeuchi, A. C. Marschilok, and K. J. Takeuchi *Coord. Chem. Rev.*, vol. 15, p. 287, 2015.

[79] B. Lee, H. R. Lee, H. Kim, K. Y. Chuang, B. W. Cho, and S. H. Oh *Chem. Commun.*, vol. 51, p. 9265, 2015.

[80] A. Ponrouch, C. Frontera, F. Barde, and M. R. Palacin *Nat. Mater.*, vol. 15, pp. 169–172, 2016.

[81] M. Chiku, H. Takeda, S. Matsumura, E. Higuchi, and H. Inoue *ACS Appl. Mater. Interfaces*, vol. 7, pp. 24385–24389, 2015.

[82] M. Angell, C. J. Pan, Y. M. Rong, C. Yuan, M. C. Lin, B. J. Hwang, and H. J. Dai *PANS*, vol. 114, pp. 834–839, 2017.

[83] L. D. Reed and E. Menke *J. Electrochem. Soc.*, vol. 160, pp. A915–A917, 2013.

[84] J. V. Rani, V. Kanakaiah, T. Dadmal, M. S. Rao, and S. Bhavanarushi *J. Electrochem. Soc.*, vol. 160, pp. A1781–A1784, 2013.

[85] S. Liu, J. Hu, N. Yan, G. Pan, G. Li, and X. Gao *Energy Environ. Sci.*, vol. 5, pp. 9743–9746, 2012.

[86] M. C. Lin, M. Gong, B. G. Lu, Y. P. Wu, D. Y. Wang, M. Y. Guan, M. Angell, C. X. Chen, J. Yang, B. J. Hwang, and H. J. Dai *Nature*, vol. 520, pp. 325–328, 2015.

[87] Z. H. Wang, S. M. Selbach, and T. Grande *RSC Adv.*, vol. 4, pp. 4069–4079, 2014.

[88] T. Placke, O. Fromm, S. F. Lux, P. Bieker, S. Rothermel, H. W. Meyer, S. Passerini, and M. Winter *J. Electrochem. Soc.*, vol. 159, p. 1755, 2012.

[89] X. Zhang, N. Sukpirom, and M. M. Lerner *Mater. Res. Bull.*, vol. 34, pp. 363–372, 1999.

[90] P. Bhauriyal, A. Mahata, and B. Pathak *Phys. Chem. Chem. Phys.*, vol. 19, pp. 7980–7989, 2017.

[91] Y.-R. Gao, C.-Q. Zhu, Z.-Z. Chen, and G. Lu *J. Phys. Chem. C*, vol. 121, pp. 7131–7138, 2017.

[92] S. C. Jung, Y.-J. Kang, D.-J. Yoo, J. W. Choi, and Y.-K. Han *J. Phys. Chem. C*, vol. 120, pp. 13384–13389, 2016.

[93] C.-J. Pan, C.-Z. Yuan, G.-Z. Zhu, Q. Zhang, C.-J. Huang, M.-C. Lin, M. Angell, B.-J. Hwang, P. Kaghazchi, and H.-J. Dai *PNAS*, vol. 115, pp. 5670–5675, 2018.

[94] M. Born and J. R. Oppenheimer *Annalen der Physik*, vol. 84, pp. 457–484, 1927.

[95] V. A. Fock *Zeitschrift fur Physik*, vol. 61, pp. 126–148, 1930.

[96] C. C. J. Roothaan *Rev. Mod. Phys.*, vol. 23, pp. 69–89, 1951.

[97] C. Møller and M. S. Plesset *Phys. Rev.*, vol. 46, pp. 618–622, 1934.

[98] K. Raghavachari and J. A. Pople *Int. J. Quantum Chem.*, vol. 14, pp. 91–100, 1978.

[99] D. Maurice and M. Head-Gordon *Mol. Phys.*, vol. 96, pp. 1533–1541, 1999.

[100] G. D. Purvis and R. J. Bartlett *J. Chem. Phys.*, vol. 76, pp. 1910–1919, 1982.

[101] L. H. Thomas *Proc. Cambridge Phil. Soc*, vol. 23, pp. 542–548, 1927.

[102] E. Fermi *Rend. Accad. Naz. Lincei*, vol. 6, pp. 602–607, 1927.

[103] P. A. M. Dirac *Proc. Cambridge Phil. Soc.*, vol. 26, p. 376, 1930.

[104] P. Hohenberg and W. Kohn *Phys. Rev.*, vol. 136, p. B864, 1964.

[105] W. Kohn and L. J. Sham *Phys. Rev.*, vol. 140, pp. A1133–A1138, 1965.

[106] R. G. Parr and W. Yang, *Density-Functional Theory of Atoms and Molecules*. Oxford University Press, 1994.

[107] P. A. M. Dirac *Proc. Cambridge Phil. Roy. Soc.*, vol. 26, pp. 376–385, 1930.

[108] S. H. Vosko, L. Wilk, and M. Nusair *Can. J. Phys.*, vol. 58, p. 1200, 1980.

[109] U. von Barth and L. Hedin *J. Phys. C: Solid State Phys*, vol. 5, pp. 1629–1642, 1972.

[110] D. C. Langreth and M. J. Mehl *Phys. Rev. B*, vol. 28, p. 1809, 1983.

[111] K. Burke, J. P. Perdew, and Y. Wang, *Derivation of a Generalize Gradient Approximation: The pw91 density functional*. Springer, Boston, MA, 1998.

[112] J. P. Perdew *Phys. Rev. B*, vol. 33, pp. 8822–8824, 1986.

[113] J. P. Perdew, K. Burke, and M. Ernzerhof *Phys. Rev. Lett.*, vol. 77, p. 3865, 1996.

[114] J. Hubbard *Proc. Roy. Soc. Lond. A*, vol. 276, pp. 238–257, 1963.

[115] A. I. Liechtenstein, V. I. Anisimov, and J. Zaanen *Phys. Rev. B*, vol. 52, pp. R5467–R5470, 1995.

[116] S. L. Dudarev, G. A. Botton, S. Y. Savrasov, C. J. Humphreys, and A. P. Sutton *Phys. Rev. B*, vol. 57, pp. 1505–1509, 1998.

[117] M. Elstner, P. Hobzy, T. Frauenheim, S. Suhai, and E. Kaxiras *J. Chem. Phys.*, vol. 114, p. 5149, 2001.

[118] S. Grimme *J. Comput. Chem.*, vol. 25, p. 1463, 2004.

[119] Y. Andersson, D. C. Langreth, and B. I. Lundqvist *Phys. Rev. Lett.*, vol. 76, p. 102, 1996.

[120] D. C. Langreth, M. Dion, H. Rydberg, E. Schröder, P. Hyldgaard, and B. I. Lundqvist *Int. J. Quantum Chem.*, vol. 101, p. 599, 2005.

[121] O. A. von Lilienfeld, I. Tavernelli, U. Röthlisberger, and D. Sebastiani *Phys. Rev. Lett.*, vol. 93, p. 153004, 2004.

[122] Y. Zhao and D. G. Truhlar *Acc. Chem. Res.*, vol. 41, p. 157, 2008.

[123] S. Grimme, S. Ehrlich, and L. Goerigk *J. Comp. Chem.*, vol. 32, p. 1456, 2011.

[124] J. C. Slater *Phys. Rev.*, vol. 36, p. 57, 1930.

[125] S. F. Boys *Proc. R. Soc. London A.*, vol. 200, p. 542, 1950.

[126] N. W. Ashcroft and N. D. Mermin. Solid State Physics, 1976.

[127] H. J. Monkhorst and J. D. Pack *Phys. Rev. B*, vol. 13, pp. 5188–5192, 1976.

[128] U. von Barth and C. D. Gelatt *Phys. Rev. B*, vol. 21, p. 2222, 1980.

[129] H. Hellmann *J. Chem. Phys.*, vol. 3, p. 61, 1935.

[130] P. Schwerdtfeger *ChemPhysChem*, vol. 12, pp. 3143–3155, 2011.

[131] M. C. Payne, M. P. Teter, D. C. Allan, T. A. Arias, and J. D. Joannopoulos *Rev. Mod. Phys.*, vol. 64, pp. 1045–1097, 1992.

[132] D. R. Hamann, M. Schlüter, and C. Chiang *Phys. Rev. Lett.*, vol. 43, pp. 1494–1497, 1979.

[133] G. B. Bachelet, D. R. Hamann, and M. Schlüter *Phys. Rev. B*, vol. 26, pp. 4199–4228, 1982.

[134] P. Blöch *Phys. Rev. B*, vol. 50, p. 17953, 1994.

[135] G. Kresse and J. Joubert *Phys. Rev. B*, vol. 59, p. 1758, 1999.

[136] D. Vanderbilt *Phys. Rev. B*, vol. 41, pp. 7892–7895, 1990.

[137] D. Jacques *Springer*, vol. 43, pp. 225–249, 1991.

[138] J. Callaway and H. C. von Baeyer *Phys. Rev.*, vol. 120, p. 1149, 1960.

[139] K. Q. Chen, W. X. Li, W. Duan, Z. Shuai, and B. L. Gu *Phys. Rev. B*, vol. 72, p. 045422, 2005.

[140] J. Maler *J. Electrochem. Soc.*, vol. 134, pp. 1524–1535, 1987.

[141] S. B. Zhang and J. E. Northrup *Phys. Rev. B*, vol. 41, pp. 2339–2342, 1991.

[142] C. Freysoldt, J. Neugebauer, and C. G. V. de Walle *Phys. Rev. Lett.*, vol. 102, p. 016402, 2009.

[143] C. Freysoldt, J. Neugebauer, and C. G. V. de Walle *Phys. Status Solidi B*, vol. 248, pp. 1067–1076, 2011.

[144] E. Fermi *Rendiconti Lincei*, vol. 3, pp. 145–149, 1926.

[145] P. A. M. Dirac *Proc. Royal Soc. Lond.*, vol. 112, pp. 661–677, 1926.

[146] P. Heitjans and J. Karger, *Diffusion in Condensed Matter: Methods, Materials, Models*. Springer Berlin Heidelberg, 2006.

[147] P. G. Bruce, *Solid state electrochemistry*. Cambridge University Press, 1997.

[148] M. Park, X. C. Zhang, M. Chung, G. B. Less, and A. M. Sastry *J. Power Sources*, vol. 195, pp. 7904–7929, 2010.

[149] G. Henkelman and H. Jonsson *J. Chem. Phys.*, vol. 113, pp. 9978–9985, 2000.

[150] H. P. Myers, *Introductory Solid State Physics*. Taylor and Francis, 2002.

[151] C. T. Chantler *J. Phys. Chem. Ref. Data*, vol. 24, pp. 71–643, 1995.

[152] C. T. Chantler *J. Phys. Chem. Ref. Data*, vol. 29, pp. 597–1048, 2000.

[153] Z. Berant, R. Moreh, and S. Kahane *Phys. Lett. B*, vol. 69, pp. 281–283, 1997.

[154] D. Waasmaier and A. Kirfel *Acta Crystallogr., Sect. A: Found. Crystallogr.*, vol. A51, pp. 416–431, 1995.